Optimal disturbances in boundary layer flows.

by

Martin G. Byström

June 2007
Technical Reports from
KTH Mechanics
SE-100 44 Stockholm, Sweden

Akademisk avhandling som med tillstånd av Kungliga Tekniska Högskolan i Stockholm framlägges till offentlig granskning för avläggande av teknologie licentiatexamen tisdagen den 12 juni 2007 kl 10.00 i sal D41, Kungliga Tekniska Högskolan, Vallhallavägen 79, Stockholm.

Universitetsservice US–AB, Stockholm 2007

Optimal disturbances in boundary layer flows.

Martin G. Byström
KTH Mechanics, SE-100 44 Stockholm, Sweden

Abstract

This thesis deals with algebraic growth in boundary layer flows, within the spatial framework. Adjoint-based optimization procedures are employed to identify the initial disturbance which experiences the maximum amplification. Such optimal disturbances are herein calculated in various boundary layer flows. Firstly, two-dimensional boundary layers affected by suction is considered, and comparisons are made between a developing boundary layer, where the leading edge region is unaffected by suction, and a non-developing boundary layer where suction is applied over the entire streamwise interval. Based on the numerical results, a hypothesis is presented to explain previous experimental findings which indicates that the spanwise scale of the disturbances is set in the leading-edge region. Secondly, swept boundary layers subjected to adverse and favourable pressure gradients are considered. It is shown that the optimal disturbances take the form of tilted vortices in the cross-flow plane. As these algebraically growing disturbances evolve downstream, they are fed into exponentially growing cross-flow modes when the critical Reynolds number is exceeded. It is also shown that the basic shape of the disturbance remains the same as it evolves from the region of algebraic growth to the super-critical region of the boundary layer.

Descriptors: Optimal disturbance, boundary layer, suction, streaks, algebraic growth, stability, transition.

Preface

The thesis contains the following papers:

Paper 1. Martin G. Byström, Ori Levin & Dan S. Henningson. *Optimal disturbances in suction boundary layers. Eur. J. Mech., B/Fluids* **26**, 330–343.

Paper 2. Martin G. Byström, Ardeshir Hanifi & Dan S. Henningson. *Optimal disturbances in the Falkner–Skan–Cooke boundary layers.* To be submitted

Division of work between authors

The numerical code employed for the first paper was already existing at KTH mechanics. Martin Byström implemented new subroutines for the baseflow and wrote the paper with assistance from Ori Levin and Dan Henningson. In the second paper, the adjoint NOLOT code, developed at FOI and DLR, was modified for the calculation of optimal disturbances by Martin Byström, who wrote the paper with assistance from Ardeshir Hanifi and Dan Henningson.

Contents

Abstract iii

Preface iv

Chapter 1. Introduction 1

Chapter 2. Suction boundary layers 3

Chapter 3. Swept boundary layers 8

Acknowledgements 15

Paper 1 19

Paper 2 43

CHAPTER 1

Introduction

The transition from laminar to turbulent boundary layer flow may follow different scenarios depending on the outside disturbance environment. Exponentially growing waves arise in boundary layers subjected to low levels of free-stream turbulence, Tollmien–Schlichting waves in two-dimensional flows and cross-flow disturbances in three-dimensional boundary layers. The breakdown of these waves causes transition. Another transition scenario may however occur in boundary layers subjected to high or moderate levels of free-stream turbulence. This kind of disturbance environment gives rise to elongated, streamwise-oriented structures of alternating low and high velocity. These structures are commonly referred to as streaks or Klebanoff modes after the experiments of Klebanoff (1971). A number of experimental studies have shown that these streaks grow algebraically in the downstream direction (Westin *et al.* (1994); Matsubara & Alfredsson (2001); Fransson *et al.* (2005)). Further, as their amplitude reach a critical level, the streaks break down to turbulence due to secondary instability (Andersson *et al.* (2001); Brandt & Henningson (2002); Hœpffner *et al.* (2005)). The theoretical framework which deals with the growth of streaks is relatively modern. Ellingsen & Palm (1975) showed that 3D disturbances can attain linear growth over time in inviscid channel flow, even when the flow does not posses any inflection point and thus is stable according to classical eigenvalue analysis. The inviscid, algebraic growth will eventually die out exponentially through viscous dissipation, as concluded by Hultgren & Gustavsson (1981). This instability is therefore denoted algebraic or transient growth. Landahl (1975,1980) illuminated the physical mechanism behind transient growth, arguing that when a fluid element is lifted up in the wall-normal direction it will initially maintain its horizontal momentum. Hence, small perturbations in the wall-normal direction can cause large disturbances in the streamwise direction. This mechanism, commonly referred to as the *lift-up* effect, is responsible for the formation of streamwise streaks.

The concept of optimal disturbances relates to various methods to identify the initial disturbance which maximizes the disturbance energy growth G, defined as

$$G = \frac{E_2}{E_1} \tag{1.1}$$

where E denotes a norm of the disturbance energy. Within the temporal framework one seeks to maximize the growth over a given time interval, E_1 thus denotes the initial disturbance energy at time zero and E_2 the energy at the end of the temporal interval. Within the spatial framework, studied in this thesis, the growth is maximized over a given streamwise interval, where E_1 denotes the energy at the inlet and E_2 the energy at the outlet. Among the first to calculate optimal disturbances numerically were Butler & Farrell (1992) and Reddy & Henningson (1993). They considered the temporal development of three-dimensional disturbances in shear flows and calculated the optimal disturbance by optimizing over the eigenmodes of the Squire and Orr–Sommerfeld operator. It was found that these disturbances consist of streamwise vortices that give rise to streamwise streaks. Luchini (1996) studied the algebraic growth of three-dimensional, spanwise periodic disturbances in the Blasius boundary layer. He concluded that a mode with unbounded growth exists in the spatially broadening boundary layer, where the effect of viscosity weakens with distance. The study was however restricted to small spanwise wavenumbers, making it impossible to determine the wavenumber associated with maximum energy growth. This optimal wavenumber was later determined by Andersson *et al.* (1999) and Luchini (2000), who independently calculated the optimal disturbance in the developing Blasius boundary layer. They employed an adjoint-based optimization procedure to calculate the optimal disturbance. In the current thesis we will employ such optimization procedures to identify the optimal disturbances in boundary layers affected by suction as well as in swept boundary layer flows.

CHAPTER 2

Suction boundary layers

Paper 1 deals with the energy growth of non-modal disturbances in boundary layers subjected to wall-suction. An adjoint-based optimization procedure is employed to identify the initial disturbance associated with the maximum energy growth, i.e. the optimal disturbance.

Fransson & Alfredsson (2003) carried out an experimental study of streaks induced into a flat plate boundary layer by free-stream turbulence. Suction was applied through the porous plate, the leading edge was however manufactured from a solid material and thus free from suction. This setup, shown in figure 2.1, resulted in the formation of a Blasius boundary layer in the upstream region, i.e. from the leading to the edge between the solid and the porous plates. Downstream of this edge, where suction was applied, the flow evolved into the asymptotic suction boundary layer (ASBL) which was reached within the upstream half of the measurement interval. Herein, we will denote this boundary layer a semi suction boundary layer (SSBL). The optimal disturbances are calculated for both the SSBL and the ASBL, and comparisons are made between these two base flows as well as with experimental results from Fransson & Alfredsson (2003). The Reynolds number is set to $Re = -U_\infty/V_\mathrm{w} = 347$ where U_∞ is the free-stream velocity and V_w is the suction velocity, as shown in figure 2.1. The scaling is described in detail in Paper 1, it is however useful to note that the streamwise coordinate x is scaled such that the suction starts at $x = 1$ in the SSBL.

In all calculations, the initial disturbance was introduced at the leading edge. The streamwise position of the outlet was varied and the optimal energy growth was calculated for streamwise intervals of varying length, as displayed in figure 2.2. It was found that the maximum growth in the SSBL occurs when the outlet is placed at the streamwise position where the suction starts, i.e. over the upstream interval unaffected by suction. This is a result of the relatively high suction rate employed by Fransson & Alfredsson (2003), with lower suction rates the optimal energy growth will increase in the downstream region affected by suction.

As expected, the optimal disturbances take the form of counter rotating, streamwise oriented vortices, portrayed in figure 2.3. The vortices grow in size and the cores become more distanced from the wall as the streamwise

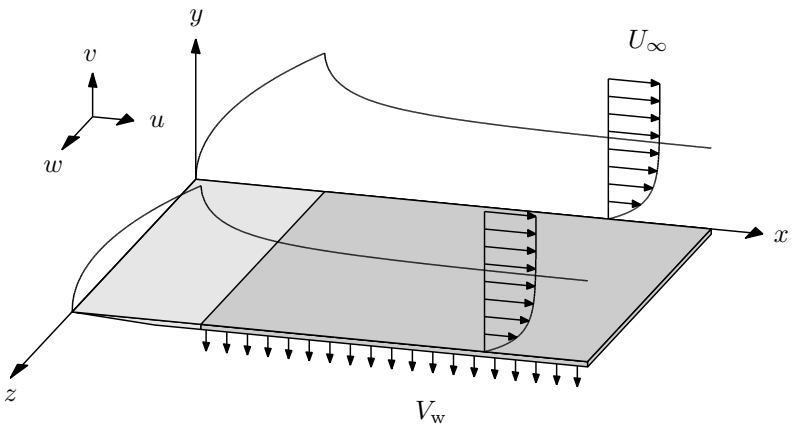

FIGURE 2.1. The semi suction boundary layer (SSBL).

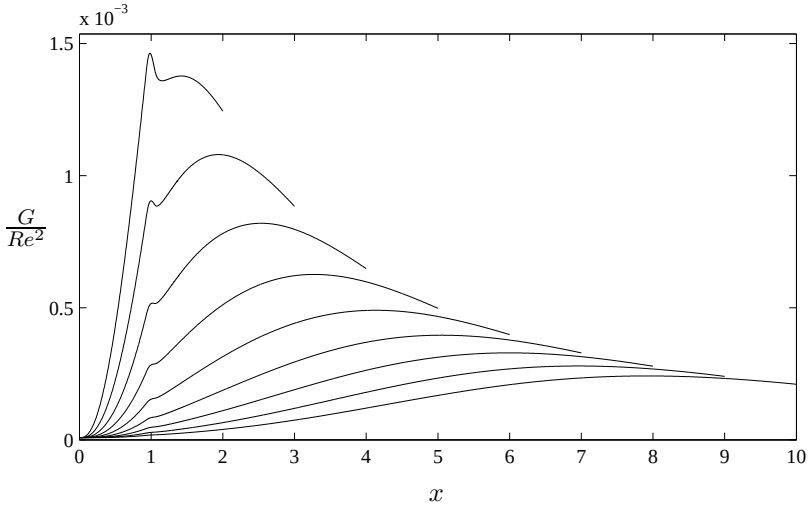

FIGURE 2.2. The growth G in the SSBL as function of the streamwise coordinate x. The optimal spanwise wavenumber of each respective interval was used, the frequency was set to zero.

interval is prolonged. A comparative study between the SSBL and the ASBL showed that the vortex cores of the optimal disturbance is located slightly higher above the wall in the ASBL, while the downstream responses collapse in long streamwise intervals. Figure 2.4 displays the energy growth in the SSBL and the ASBL as function of both the spanwise wavenumber and the streamwise coordinate. It was concluded that the energy growth as well as

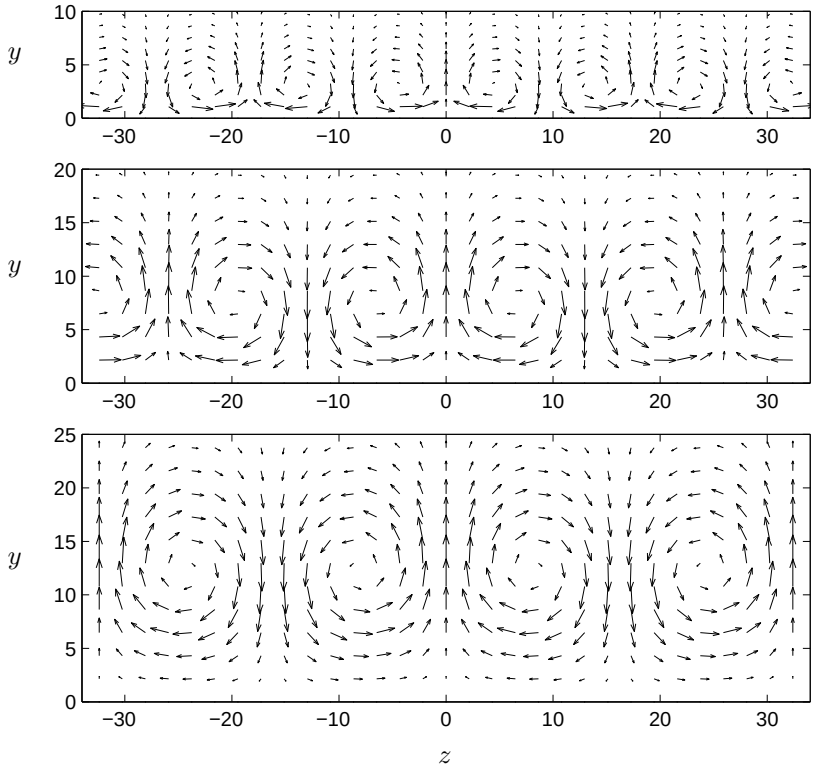

FIGURE 2.3. The optimal disturbance in the SSBL for the streamwise intervals $0 \leq x \leq 2$ (upper row), $0 \leq x \leq 6$ (middle row) and $0 \leq x \leq 10$ (bottomrow).

the optimal spanwise wavenumber in the SSBL approach that in the ASBL when the streamwise interval is prolonged. The energy growth is however significantly higher in the SSBL over short intervals. These spatial results were also compared to a previous temporal study of algebraic growth in the ASBL by Fransson & Corbett (2003). It was found that the spatial methodology predicts a maximum energy growth which is 16% higher than the temporal result, the optimal spanwise wavenumber was however nearly identical.

There are a numbers of factors which need to be considered when comparing the calculations presented herein to experimental results. In the calculations, we assume that the disturbance enter the boundary layer at the initial point of the streamwise interval and then evolves downstream without any influence from the outside disturbance environment. This in in contrast to the experimental conditions where the boundary layer is subjected to continuous forcing from the free-stream turbulence over the entire streamwise interval. There

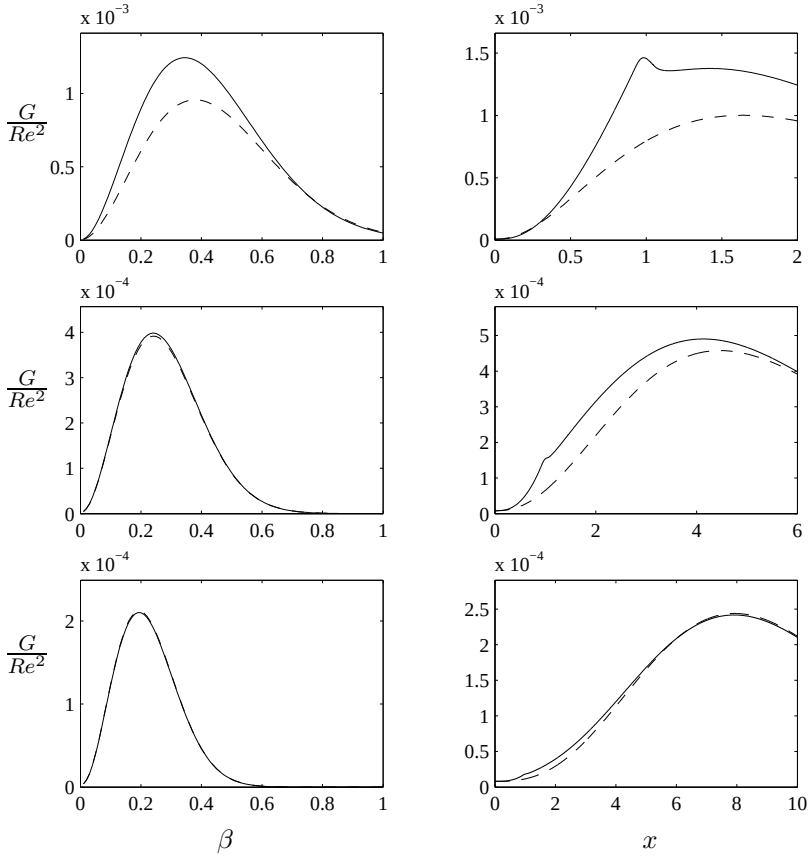

FIGURE 2.4. Left column: the growth G as function of the spanwise wavenumber β. Right column: the growth of the disturbance with optimal wavenumber as function of the streamwise coordinate x. The SSBL (solid line) and the ASBL (dashed line). The upper, middle and bottom row shows the growth in the streamwise intervals $0 \leq x \leq 2$, $0 \leq x \leq 6$ and $0 \leq x \leq 10$, respectively.

is also the possibility for nonlinear effects, which are not accounted for with linearized equations employed herein. The calculations do however provide a possible explanation for experimental findings which show that the spanwise scale of the streaks in the SSBL is close to the scale of the streaks in the Blasius boundary layer where no suction is applied. The present study has shown that the relatively high suction rate makes it impossible for disturbances of the optimal scale in the ASBL to grow in the downstream region affected by suction.

This region will therefore be dominated by streaks of scales close to the optimal scale in the Blasius boundary layer, since these disturbances have already grown to large amplitudes in the upstream region unaffected by suction.

CHAPTER 3

Swept boundary layers

In paper 2, we continue our study of algebraic instability in boundary layer flows. The scene of the survey has changed to the three-dimensional (3D) boundary layer over a flat, swept plate, where a constant pressure gradient is present in the chordwise direction. The flow is independent of the spanwise coordinate, this type of 3D flow is often referred to as 2.5D. For the incompressible flow studied herein, the boundary layer is described by the Falkner–Skan–Cooke similarity solution. The sweep angle is set to 45°, both adverse and favorable pressure gradients are considered. A parabolic set of disturbance equations are employed to study the algebraic growth of spanwise periodic, stationary disturbances with infinite wave length in the propagation direction. Both sub- and supercritical Reynolds numbers are considered. An adjoint-based optimization procedure is employed to calculate the optimal disturbances and the associated energy growth. For the figures presented in this chapter, two coordinate systems are employed. The coordinates r^1 and r^2 are aligned with and perpendicular to the incoming flow, respectively, while the coordinates s^1 and s^2 are aligned with and perpendicular to the external streamline. The wall-normal coordinate is denoted by r^3 and s^3. Further details on the coordinate systems and scaling are given in Paper 2.

It is well known that disturbances in 3D boundary layers tend to be aligned with the external streamline. The disturbance equations were therefore integrated along this line, and the wavenumber in this direction was set to zero. The disturbances were however found to deviate a small amount from the streamline, as shown in figure 3.1. An iterative procedure was therefore implemented, where the true propagation direction of the disturbance is identified and employed as integration path. This line, which we denote the *streakline*, is defined as the line which follows the maximum of the streamwise component of the disturbance velocity.

First a sub-critical streamwise interval was considered and the optimal disturbances calculated. Figure 3.2 shows the optimal disturbances at the inlet and the resulting streaks at the outlet. In agreement with what has been found for a number of 2D shear flows, the optimal disturbances takes the form of counter rotating vortices, when the disturbances are projected onto the cross-flow plane

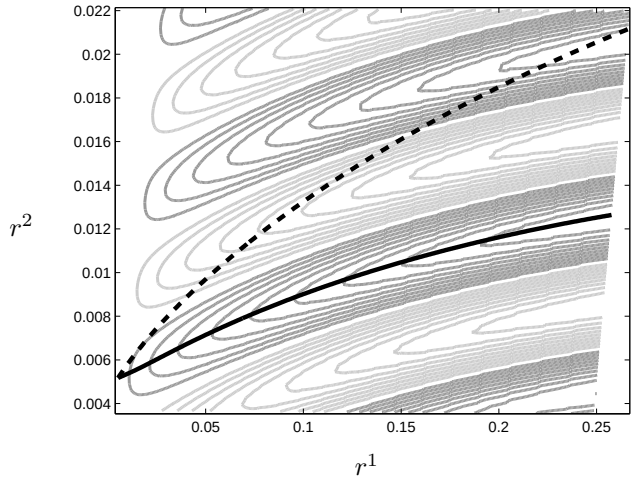

FIGURE 3.1. Contours of positive (dark gray) and negative (light gray) streamwise velocity. External streamline (dashed line) and the streakline (solid line) used in the calculations, following the maximum of the streamwise disturbance velocity. Note that the figure does not portray one plane at a fixed wall-normal position, but rather a curved sheet which follows the maximum of the streamwise disturbance velocity at each chordwise station. Note also the high visual aspect ratio between the r^1- and r^2-axis.

(i.e. the plane perpendicular to the external streamline). The vortices are however not symmetric as in 2D flows, but tilted around the wall-normal axis. The vortices are tilted anti-clockwise in the accelerated flow and clockwise in the retarded flow. This difference is likely related to the cross-flow component of the boundary layer, which changes sign with the pressure gradient. The vortices gives rise to streaks of alternating low and high streamwise velocity (here streamwise denotes the direction of the external streamline). These streaks at the outlet are also displayed in figure 3.2, we gather that the orientation of the disturbances change as they evolve downstream, such that the streaks in the accelerated flow is tilted clockwise at the outlet while the streaks in the retarded flow are tilted anti-clockwise.

Secondly, the streamwise interval for the accelerated flow was extended to include super-critical Reynolds numbers. The optimal disturbance and the corresponding energy growth was calculated for this interval. Figure 3.3 shows the energy growth of the optimal disturbances, the algebraic growth at the upstream part of the interval pass over to exponential growth as the critical

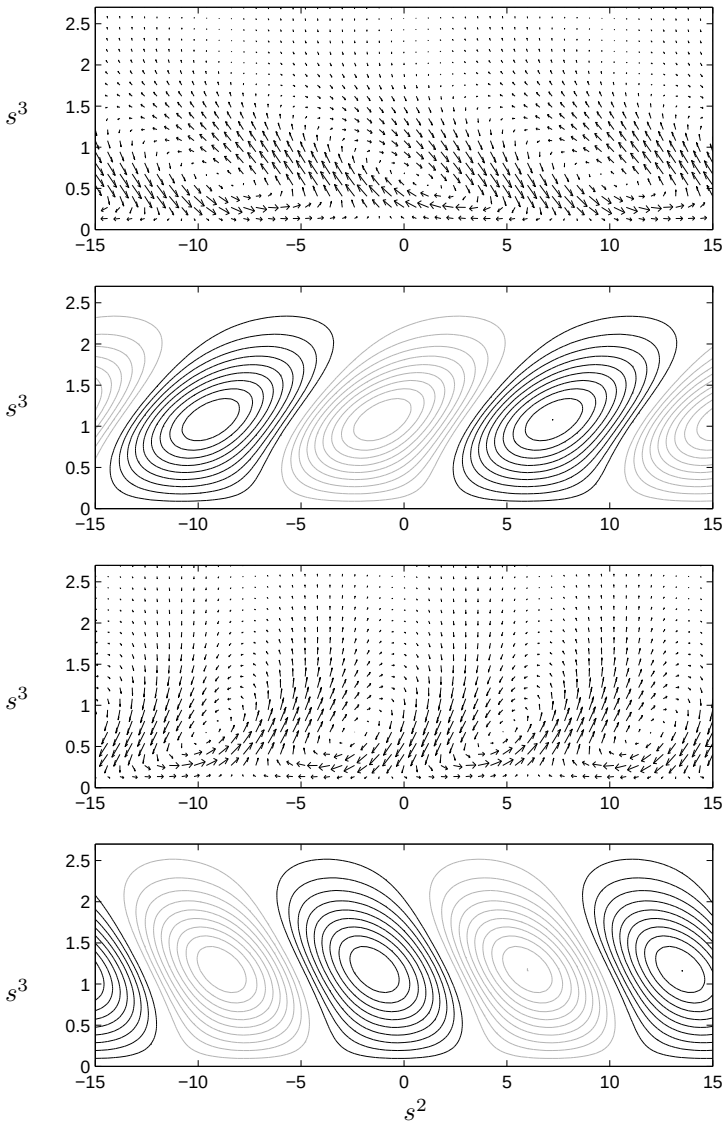

FIGURE 3.2. (a & c) Vector representation of optimal disturbances in the Falkner–Skan boundary layers, projected onto the cross-flow plane at the inlet. (c & d) Downstream response to the optimal disturbances, contours of positive (black) and negative (grey) streamwise velocity in the cross-flow plane. (a & b), Favorable pressure gradient. (c & d) Adverse pressure gradient.

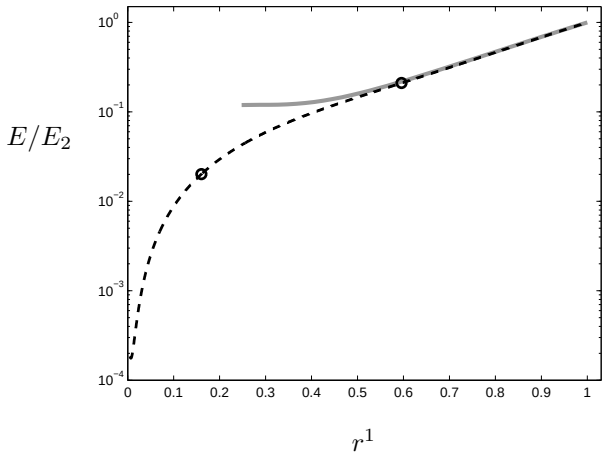

FIGURE 3.3. Energy growth of the optimal disturbance (black dashed line), algebraic growth followed by exponential growth. Data from a PSE calculation of a cross-flow mode (grey line) with the same spanwise wavenumber is included for comparison. The dots are associated with figure 3.4.

Reynolds number is surpassed. Data from a calculation with parabolized stability equations for a cross-flow mode initiated at the neutral stability point has been included for comparison. It can be seen that the growth rate of the optimal disturbance collapse with that of the cross-flow mode in the super-critical part of the interval. The disturbance profiles of the downstream response of the optimal disturbance collapse perfectly with the profiles of the cross-flow mode at the outlet (see figure 11 in paper 2). Hence, it was concluded that the algebraically growing, non-modal disturbance pass over into an exponentially amplified cross flow mode as the critical Reynolds number is surpassed. From figure 3.3 it can also be concluded that the transition from algebraic to exponential growth is a gradual process without any jumps in the growth rate. Figure 3.4 portrays the amplitude functions at two streamwise stations, marked in figure 3.3, where the disturbances receives algebraic and exponential amplification, respectively. It is clear that no dramatic change has occurred to the shape of the disturbance. It was therefore concluded that the physical mechanism that drives the algebraic instability is similar to that responsible for the exponential instability, and that the algebraic disturbances are feed into exponentially amplified modes as the critical Reynolds-number is exceeded.

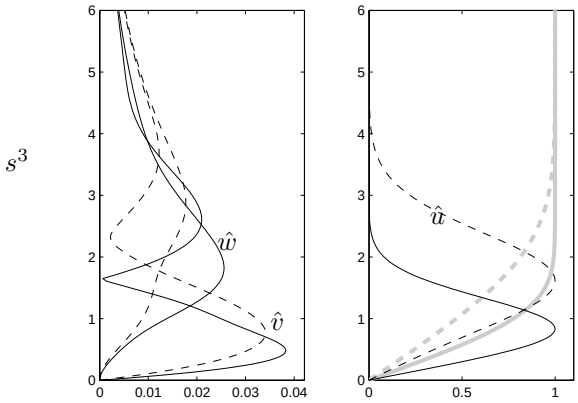

FIGURE 3.4. Downstream response to the optimal disturbance in regions of algebraic (solid line) and exponential growth (dashed line), i.e. the chordwise positions marked by dots in figure 3.3. Falkner–Skan–Cooke profiles at the same positions (grey line). The chordwise, spanwise and wall-normal velocity component are denoted u, v and w, respectively.

References

Andersson, P., Berggren, M. & Henningson, D. 1999 Optimal disturbances and bypass transition in boundary layers. *Phys. Fluids* **11** (1), 134–150.

Andersson, P., Brandt, L., Bottaro, A. & Henningson, D. S. 2001 On the breakdown of boundary layer streaks. *J. Fluid Mech.* **428**, 29–60.

Brandt, L. & Henningson, D. S. 2002 Transition of streamwise streaks in zero-pressure-gradient boundary layers. *J. Fluid Mech.* **472**, 229–261.

Butler, K. M. & Farrell, V. F. 1992 Three-dimensional optimal perturbations in viscous shear flow. *Phys. Fluids A* **4** (8), 1637–1650.

Ellingsen, T. & Palm, E. 1975 Stability of linear flow. *Phys. Fluids* **18** (4), 487–488.

Fransson, J. H. M. & Alfredsson, P. H. 2003 On the disturbance growth in an asymptotic suction boundary layer. *J. Fluid Mech.* **482**, 51–90.

Fransson, J. H. M. & Corbett, P. 2003 Optimal linear growth in the asymptotic suction boundary layer. *Eur. J. Mech., B/Fluids* **22**, 259–270.

Fransson, J. H. M., Matsubara, M. & Alfredsson, P. H. 2005 Transition induced by free-stream turbulence. *J. Fluid Mech.* **527**, 1–25.

Hœpffner, J., Brandt, L. & Henningson, D. S. 2005 Transient growth on boundary layer streaks. *J. Fluid Mech.* **537**, 91–100.

Hultgren, L. & Gustavsson, L. 1981 Algebraic growth of disturbances in a laminar boundary layer. *Phys. Fluids* **24** (6), 1000–1004.

Klebanoff, P. S. 1971 Effect of freestream turbulence on the laminar boundary layer. *Bull. Am. Phys. Soc.* **10**, 1323.

Luchini, P. 1996 Reynolds-number-independent instability of the boundary layer over a flat surface. *J. Fluid Mech.* **327**, 101–115.

Luchini, P. 2000 Reynolds-number-independent instability of the boundary layer over a flat surface: optimal perturbations. *J. Fluid Mech.* **404**, 289–309.

Matsubara, M. & Alfredsson, P. H. 2001 Disturbance growth in boundary layers subjected to free-stream turbulence. *J. Fluid Mech.* **430**, 149–168.

Reddy, S. C. & Henningson, D. S. 1993 Energy growth in viscous channel flows. *J. Fluid Mech.* **252**, 209–238.

Westin, K. J. A., Boiko, A. V., Klingmann, B. G. B., Kozlov, V. V. & Alfredsson, P. H. 1995 Experiments in a boundary layer subjected to free

stream turbulence. Part 1. Boundary layer structure and receptivity. *J. Fluid Mech.* **281**, 193–218.

Acknowledgements

I thank my supervisors Professor Dan Henningson, who gave me the opportunity for these studies, and Professor Ardeshir Hanifi who has guided me through the work. I also thank Ori Levin who was my advisor during my first time at the department.

I thank Docent Jens Fransson for many valuable comments on Paper 1. I also thank Doctor Jan Pralits for his advice.

Furthermore, I like to thank everyone at department, in particular my colleagues Carl-Gustav, Shervin, Luca, Lars-Uve, Astrid, Ori, Espen, Jérôme, Mattias, Erik and Philipp.

I gratefully acknowledge the financial support from the EU project TELFONA.

Part II

Papers

1

Paper 1

Optimal disturbances in suction boundary layers

By Martin G. Byström, Ori Levin and Dan S. Henningson

A well known optimization procedure is used to find the optimal disturbances in two different suction boundary layers within the spatial framework. The maximum algebraic growth in the asymptotic suction boundary layer is presented and compared to previous temporal results. Furthermore, the spatial approach allows a study of a developing boundary layer in which a region at the leading edge is left free from suction. This new flow, which emulates the base flow of a recent wind-tunnel experiment, is herein denoted a semi suction boundary layer. It is found that the optimal disturbances for these two suction boundary layers consist of streamwise vortices that develop into streamwise streaks, as previously found for a number of shear flows. It is shown that the maximum energy growth in the semi suction boundary layer is obtained over the upstream region where no suction is applied. The result indicates that the spanwise scale of the streaks is set in this region, which is in agreement with previous experimental findings.

1. Introduction

The transition from laminar to turbulent flow is a critical process in any engineering application where the minimization of friction drag is a design objective. Transition prediction has traditionally been carried out by considering the unstable eigenmodes of the Orr–Sommerfeld equations, i.e. the exponentially growing Tollmien–Schlichting waves. However, under certain circumstances other transition scenarios are more likely. It is well known that elongated, streamwise-oriented structures of alternating low and high velocity develop in boundary layers subjected to high or moderate levels of free-stream turbulence. These structures are commonly referred to as streaks or Klebanoff modes after the experiments of Klebanoff (1971). Since then, a number of experimental studies have shown that these streaks grow algebraically in the downstream direction (Westin *et al.* (1994); Matsubara & Alfredsson (2001); Fransson *et al.* (2005)). Due to secondary instabilities, they break down to turbulence when their amplitude reach a critical level (Andersson *et al.* (2001); Brandt & Henningson (2002); Hœpffner *et al.* (2005)). The physical mechanism behind the formation of streaks was first explained by Landahl (1975, 1980). He

argued that when a fluid element is lifted up in the wall-normal direction it will initially maintain its horizontal momentum. Hence, small perturbations in the wall-normal direction can cause large disturbances in the streamwise direction. This mechanism is commonly referred to as the *lift-up* effect. Ellingsen & Palm (1975) showed theoretically that three-dimensional disturbances can grow linearly with time in an inviscid flow without inflection point.

Among the first to calculate optimal perturbations numerically were Butler & Farrell (1992) and Reddy & Henningson (1993). Butler & Farrell (1992) considered the temporal development of linear, three-dimensional perturbations in a number of shear flows. They used a variational method to find the optimal perturbations, i.e. the perturbations that gain the most energy in a given time period. It was found that these perturbations resemble streamwise vortices that give rise to streamwise streaks. Corbett & Bottaro (2000, 2001) calculated the optimal perturbation of the Falkner–Skan boundary layer and later the Falkner–Skan–Cooke boundary layer within the temporal framework. The spatial framework is however more physically relevant than the temporal, it has also the advantage of allowing studies of non-parallel flows such as the developing Blasius boundary layer (BBL). Andersson *et al.* (1999) and Luchini (2000) separately calculated the optimal disturbance in the non-parallel BBL. The disturbance was introduced at the leading edge and it was found that the optimal disturbance consists of streamwise aligned vortex pairs developing into streaks. Levin & Henningson (2003) extended the work of Andersson *et al.* (1999) to the Falkner–Skan boundary layer. The disturbance was however not initiated at the leading edge, but at a downstream position optimized to give the highest possible growth.

One method to delay transition is to apply suction through the surface which the boundary layer develops over. The suction can be optimized to minimize the growth of different types of disturbances Balakumar & Hall (1999); Pralits *et al.* (2002); Zuccher *et al.* (2004). Herein we will however study the algebraic disturbance growth in boundary layers where uniform suction is applied. When uniform suction is applied over a flat plate, the boundary layer will asymptotically approach the asymptotic suction boundary layer (ASBL), as outlined in Schlichting (1979). Fransson & Alfredsson (2003) made an experimental study on the algebraic growth of disturbances induced by free-stream turbulence in the ASBL. A small region at the leading edge was however free from suction, allowing a BBL to develop up to the point where the suction set in. Downstream of this point the flow evolved into the ASBL, which was reached within the upstream half of the measurement interval. In the present paper, we will denote this type of boundary layer, where suction is applied only over the downstream part of the interval, a semi suction boundary layer (SSBL). Fransson & Alfredsson (2003) compared the disturbance growth in the BBL and the SSBL. The disturbance energy was found to grow linearly in the downstream direction, but when suction was applied the growth ceased

so that the present amplitude level was kept essentially constant. The suction also resulted in a twofold reduction of the boundary-layer thickness, despite of this the spanwise scale of the streaks was maintained. Fransson & Alfredsson (2003) argue that the initial spanwise scale is decided in the receptivity process, this would explain the similarity of scales since a BBL is present at the leading edge of the SSBL. Yoshioka *et al.* (2004) extended the work of Fransson & Alfredsson (2003) to a number of turbulence levels, free-stream and suction velocities. They found that the wall suction suppresses the disturbance growth, for high suction rates the disturbance energy may even decay. For conditions similar to those of the experiment by Fransson & Alfredsson (2003), it was concluded that the disturbances initiated at the leading edge become mainly passive and are convected downstream by the flow without changing the spanwise scale. However, Yoshioka *et al.* (2004) argue that the spanwise scale of the streaks approach the optimal scale in the ASBL when the conditions are such that the difference in displacement thickness between the upstream and downstream region is small. Fransson & Corbett (2003) used an adjoint-based optimization procedure (Corbett & Bottaro (2001)) to calculate the optimal perturbation in the ASBL within the temporal framework. The optimal velocity perturbation was found to be in good agreement with experimental data from Fransson & Alfredsson (2003), but there was some discrepancy between the optimal wavenumber and those experimentally observed.

In the present paper we calculate the optimal disturbances in the ASBL and the SSBL within the spatial context. The calculations are carried out with an adjoint-based optimization procedure implemented by Levin & Henningson (2003), valid in the large Reynolds-number limit for a viscous, incompressible flow. Furthermore, the spanwise wavenumber and angular frequency of the disturbance as well as the streamwise interval length are optimized. The current study was motivated by the wind-tunnel experiment by Fransson & Alfredsson (2003). Results from this experiment have previously been compared with the temporal study of the ASBL by Fransson & Corbett (2003). This study was however restricted to a non-developing base flow. The spatial approach used herein allows us to simulate the actual base flow of the experiments, i.e. the SSBL. A comparison of the optimal disturbances in the ASBL and the SSBL is then carried out to establish the effect of the differences between these two suction boundary layers.

2. General formulation

We study the growth of optimal disturbances in a flat plate boundary layer where suction is applied at the wall. As seen in figure 1, we denote the streamwise, wall-normal and spanwise coordinates x, y and z and the corresponding velocities u, v and w, respectively. The time is denoted t, the pressure p, the spanwise wavenumber and the angular frequency are denoted β and ω. The kinematic viscosity and the density of the fluid are denoted ν and ρ.

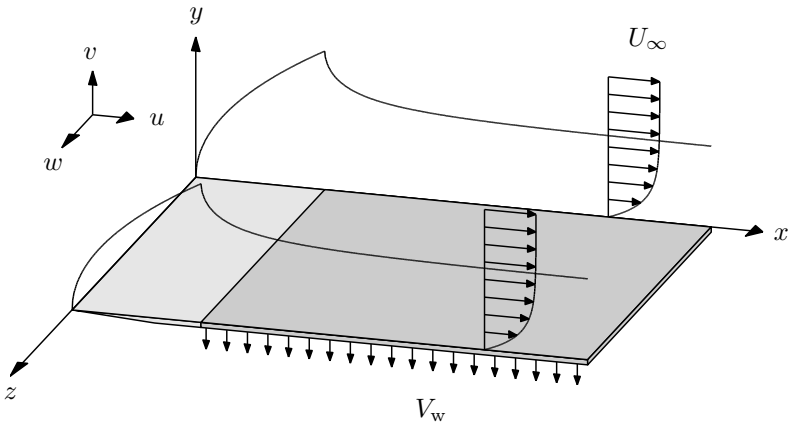

FIGURE 1. The semi suction boundary layer (SSBL).

The base flow of the ASBL is given by a simple analytic expression, first derived by Griffith and Meredith Griffith & Meredith (1936)

$$U = U_\infty \left(1 - \exp\left[\frac{V_w}{\nu} y\right]\right), \qquad V = V_w, \tag{1}$$

where U_∞ is the free-stream velocity and V_w is the suction velocity at the wall, which assumes a negative value when suction is applied. This velocity profile is an exact solution to both the full Navier–Stokes equations and the boundary-layer equations. The displacement thickness δ_1 of the ASBL is constant since the base flow does not vary in the streamwise direction. The Reynolds number based on this constant displacement thickness can also be written as the ratio between the free-stream velocity and the suction velocity, from here on we will refer to this as the suction Reynolds number Re

$$\delta_1 = -\frac{\nu}{V_w}, \quad Re = \frac{U_\infty \delta_1}{\nu} = -\frac{U_\infty}{V_w}. \tag{2}$$

Herein we will use a scaling based on the constant displacement thickness of the ASBL to scale both mean flow and disturbances. This scaling, summarized in table 1, will be referred to as the ASBL scalings. From here on we will use the superscript * to distinguish non-scaled, physical quantities from those scaled in accordance with table 1. Using scaled quantities we may rewrite equation (1)

$$U = \frac{U^*}{U_\infty} = 1 - \exp\left[-\frac{y^*}{\delta_1}\right] = 1 - \exp\left[-y\right], \qquad V = \frac{V_w^*}{U_\infty} Re = V_w. \tag{3}$$

The base flow of the SSBL can be divided into two regions. In the first region, from the leading edge to the position where the suction starts, the base flow was obtained by solving the Blasius similarity equation. In the second region, where suction is applied, the base flow was obtained by numerically solving the boundary-layer equations. The streamwise velocity is subjected to

TABLE 1. The ASBL scalings

variable:	x	y, z	t	u	v, w	p	β	ω
scaling:	$\delta_1 Re$	δ_1	$\delta_1 Re/U_\infty$	U_∞	U_∞/Re	$\rho U_\infty^2/Re^2$	$1/\delta_1$	$U_\infty/(\delta_1 Re)$

homogeneous boundary conditions at the wall, the boundary condition for the wall-normal component is given by the suction velocity V_w. We scale the SSBL with the ASBL scalings given by table 1. The Reynolds number $Re = -U_\infty/V_\mathrm{w}$ is however not physically relevant in the upstream region where no suction is applied. The BBL of this region has previously been studied by Andersson *et al.* (1999), Luchini (2000) and Levin & Henningson (2003). They used boundary-layer scalings and defined a Reynolds number $Re_l = U_\infty l/\nu$, where l is a fixed streamwise distance that is also used to scale x. In the SSBL, the natural choice for l is the distance between the leading edge and the point where the suction starts. Writing the starting position of the suction, x_s, with the ASBL scalings from table 1

$$x_\mathrm{s} = \frac{x_\mathrm{s}^*}{\delta_1 Re} = \frac{l}{\delta_1 Re} = \frac{Re_l}{Re^2}, \tag{4}$$

we find that changing the starting position of the suction is equivalent to changing Re_l, given that Re is kept constant. In the study of the SSBL presented in § 3.1 we set x_s to unity in order to comply with the experiments by Fransson & Alfredsson (2003). Setting x_s to unity is equivalent to setting $Re_l = Re^2$, this is beneficiary since it means that quantities scaled with the ASBL scalings can be directly compared to quantities scaled with the boundary-layer scalings and vice versa. Further details on the base flow of the SSBL will be given in § 3.1a.

For these two-dimensional steady base flows, the SSBL and the ASBL, we consider three-dimensional and time-dependent disturbances. The disturbances are taken to be periodic in the spanwise direction and in time. We consider algebraically growing disturbances with weak streamwise variation, the streamwise wavenumber is thus set to zero. Either one of the disturbances u, v, w or p can then be assumed to be of the form

$$f = \hat{f}(x, y) \exp\left[\mathrm{i}\beta z - \mathrm{i}\omega t\right]. \tag{5}$$

Introducing this assumption in the non-dimensional, linearized Navier–Stokes equations and neglecting terms of low order yields a parabolic set of disturbance equations as outlined in Levin & Henningson (2003). The disturbance is subjected to no-slip boundary conditions at the wall, the wall-normal disturbance can be set to zero since we consider suction through a material of low permeability (Fransson & Corbett (2003)). Together with boundary and initial

conditions, the disturbance equations form an initial boundary-value problem that can be solved through downstream marching for a disturbance with given spanwise wavenumber and angular frequency.

The aim is to optimize the initial disturbance $(\hat{u}_0, \hat{v}_0, \hat{w}_0)$ at x_0, the beginning of the interval, in order to achieve maximum possible amplification of the disturbance energy at x_1, the end of the interval. We define the growth G over the interval $x_0 \leq x \leq x_1$ as the ratio between the disturbance energy E at the end and beginning of the interval.

$$G(x_0, x_s, x_1, \beta, \omega, Re) = \frac{E(x_1)}{E(x_0)}. \tag{6}$$

Observe that the growth in the ASBL will not depend on the position where the suction starts, x_s, since we assume that it is located sufficiently far upstream so that the ASBL has been reached at the start of the interval. The energy norm E is defined in the same way as stated in Andersson *et al.* (1999), Luchini (2000) and Levin & Henningson (2003). As outlined in these papers, in a high Reynolds-number flow the highest possible growth is achieved for an initial disturbance with a zero streamwise component, due to the difference in order between the streamwise component and the wall-normal and spanwise components. This difference in order also makes it possible to neglect the wall-normal and spanwise components at the end of the interval. It then follows that the growth scales quadratically with Re in the large Reynolds-number limit (Andersson *et al.* (1999); Luchini (2000); Levin & Henningson (2003)).

Since the initial boundary-value problem is linear and homogeneous an input-output formulation can be adopted, such that the disturbance at the final position is a linear function of the initial disturbance. By introducing the adjoint equations, the optimal initial disturbance and the associated growth can be calculated through power iterations. The optimization procedure used herein to calculate the optimal disturbances in the SSBL and the ASBL was implemented by Levin & Henningson (2003). It is similar to the procedures that were used by Andersson *et al.* (1999) and Luchini (2000). A detailed description of this procedure can also be found in the textbook by Schmid, D. S. Henningson (2001).

3. Results

All results presented in this section have been subjected to convergence tests in order to ensure their accuracy. Furthermore, the height of the calculation box $y_{\max}$ was varied between 40 and 60 to make sure that the whole initial disturbance was captured.

3.1. *The semi suction boundary layer*

3.1a. *Base flow.* In this section we study the SSBL in which a BBL develops from the leading edge to the point where the suction starts. Downstream

of this point a uniform suction is applied, in this evolution region the flow evolves towards the ASBL. The streamwise distance needed for the flow to reach the ASBL is decided by the strength of the suction and the thickness of the BBL at the position where the suction starts. The SSBL emulates the base flow of an experiment carried out by Fransson & Alfredsson (2003). In this experiment, the boundary layer developed over a flat plate made of porous material so that suction could be applied. The leading edge was however made of an impermeable material, leaving this region free from suction. Fransson & Alfredsson (2003) set the suction Reynolds number to $Re = 347$ and started the suction 360 mm downstream of the leading edge, equivalent to setting $x_{\rm s} = x_{\rm s}^*/(\delta_1 Re)$ to unity. As outlined in § 2, this allows us to make direct comparisons with quantities scaled with the boundary-layer scalings. Herein we study the SSBL over nine streamwise intervals, all starting at $x_0 = 0$ and with suction from $x_{\rm s} = 1$ to the end of the interval. The length of the interval is varied by changing the end position from $x_1 = 2$ to $x_1 = 10$ in steps of one.

Fransson & Alfredsson (2003) used a non-dimensional evolution equation to calculate the base flow of the evolution region between the BBL and the ASBL. The exact agreement with their results validated the numerical solver of the boundary-layer equations that was used in the present implementation. A small modification of the base flow was however made since the SSBL is discontinuous at $x_{\rm s} = 1$ where the suction starts. In order to remove this discontinuity, we employ a strategy previously used by Zuccher *et al.* (2004) and Corbett & Bottaro (2001), using a step function to smoothly increase the suction from zero at $x = 0.9$ to full suction at $x = 1.1$. The used step function (Berlin & Henningson (1996)) has continuous derivatives of all orders and gives the same mass flux through the wall as the discontinuous flow. Figure 2 shows a comparison of the displacement thickness of the discontinuous flow and the modified continuous flow with smoothly applied suction. Despite the smooth application of the suction, the flow undergoes a significant transformation over a short streamwise distance, a finer grid was therefore used in this region and at the leading edge. Experimental data from Fransson & Alfredsson (2003) is also included in figure 2, good agreement can be seen between the calculated and measured displacement thickness.

Another approximation was done in the treatment of the leading edge. The limit of the normal velocity of the BBL is infinity when x tends towards zero. However, here we follow the work of Andersson *et al.* (1999) and set the normal velocity to zero and the streamwise velocity to unity at the initial point of the calculation interval.

3.1b. *Optimal disturbances.* The influence of the spanwise wavenumber β and the angular frequency ω on the energy growth in the SSBL was studied for the nine streamwise intervals defined in § 3.1a. Apart from when the ω-dependence is studied, ω is set to zero for all calculations presented in this section.

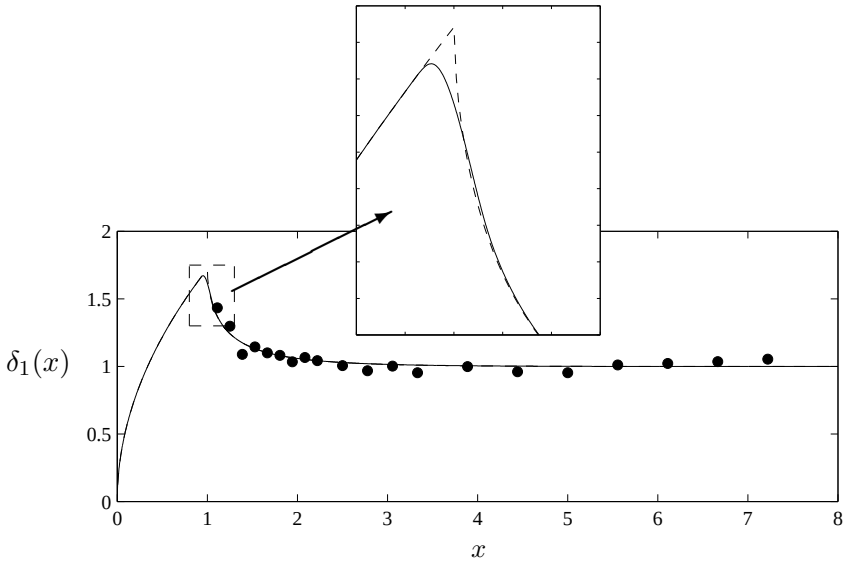

FIGURE 2. The displacement thickness $\delta_1(x)$ of the SSBL at $Re = 347$, scaled with the constant displacement thickness of the ASBL. Discontinuous flow (dashed line) and approximated continuous flow with smoothly applied suction (solid line). Experimental data from Fransson and Alfredsson Fransson & Alfredsson (2003) (dots).

Figure 3 shows the growth as function of β for all nine streamwise intervals. We gather that the optimal growth occurs at different β for each respective interval, i.e. for each streamwise interval there is an optimal β that gives the largest possible growth at the end of that interval. This optimal β and the corresponding optimal growth decrease as the interval is prolonged. The optimal spanwise wavenumbers and the corresponding optimal growth are summarized in table 2, § 3.2.

The ω-dependence is exposed in figure 4, which shows contours of constant growth in the (ω, β)-plane for the streamwise interval $0 \leq x \leq 6$. From the figure we conclude that the optimal ω is zero, this conclusion was found to be true for all the streamwise intervals studied here. This is in agreement with what has been found for the BBL by Luchini (2000) and the Falkner–Skan boundary layer by Levin & Henningson (2003).

The growth as function of the streamwise coordinate x is shown in figure 5 for all nine streamwise intervals. The optimal β of each respective interval was used in these calculations and ω was set to zero. The optimization procedure used herein optimizes the growth at the end of the streamwise interval. The

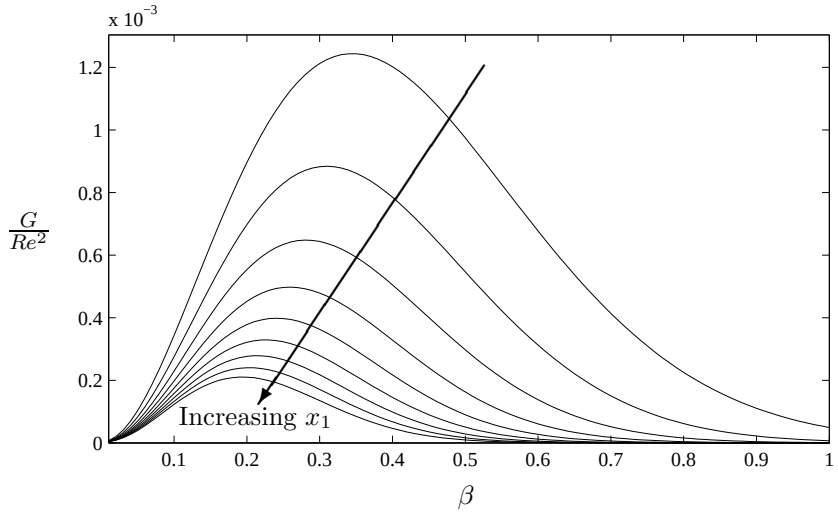

FIGURE 3. The growth G in the SSBL at $Re = 347$ as function of β for nine streamwise intervals ranging from $0 \leq x \leq 2$ to $0 \leq x \leq 10$ in steps of one.

optimal growth is thus the largest possible growth at the end of the streamwise interval but does not necessarily constitute the largest growth in the interval. As seen in figure 5 each curve has a maximum upstream of their respective end position and these maxima exceed the optimal growth for all intervals. The maxima are located in the suction part of the SSBL, except for the shortest interval ($0 \leq x \leq 2$), which has the maximum located at the starting point of the suction, i.e. at the end of the BBL. When the endpoint of the interval was moved further upstream, towards the starting point of the suction, it was found that the maximum remains located at this point. Due to the smooth application of the suction (see § 3.1a), the maximum growth is reached slightly upstream of $x_\mathrm{s} = 1$. It is however reasonable to assume that the maximum growth will be reached at exactly $x_\mathrm{s} = 1$ in the discontinuous flow. The optimal interval for the SSBL thus ends at the point where the suction starts. In this interval, where no suction is applied, the base flow is simply the BBL for which it is well known that the optimal spanwise wavenumber is $\beta = 0.45$ (Andersson *et al.* (1999), Luchini (2000)).

Figure 6 shows the optimal disturbances in the SSBL for the streamwise intervals $0 \leq x \leq 2$ (solid line), $0 \leq x \leq 6$ (dashed line) and $0 \leq x \leq 10$ (dotted line). For each respective interval the optimal β was used and ω was set to zero. Figures 6 (a–b) show the optimal disturbance while figure 6 (c) shows the downstream response of the optimal disturbance at the final position. The downstream response takes the form of a streamwise elongated streak when

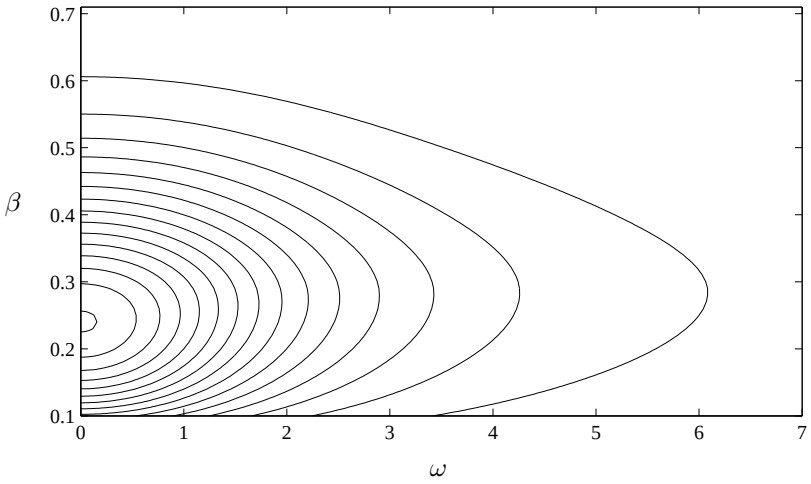

FIGURE 4. Contours of constant growth G in the SSBL at $Re = 347$ in the (ω, β)-plane for the streamwise interval $0 \leq x \leq 6$.

the spanwise periodic dependence is considered. The amplitude of the streak is larger for short intervals than for long, but the shape of the streak remains similar and the profile maximum is located at about the same wall-normal distance from the wall, where the SSBL reaches approximately three quarters of the free-stream velocity. From this we conclude that there is an optimal shape, a streak located at a certain wall-normal position, that gives the highest disturbance energy at the end of the interval.

The optimal disturbance, i.e. the wall-normal and spanwise components shown in figures 6 (a–b), takes the form of streamwise aligned vortex pairs when the spanwise periodic dependence is considered. We also observe that the profile maxima move upward when the streamwise interval is prolonged. Thus, the vortex cores of the initial disturbance move upward and the vortices grow in size, as seen in figure 7. An explanation for this is that the suction will draw the disturbance towards the wall as it evolves downstream. From figure 6 (c) we saw that the downstream response of the optimal disturbance is a streak located at a certain optimal wall-normal position. The cores of the vortices, i.e. the optimal disturbance, must be located some distance higher in the wall-normal direction in order to allow the suction to draw the disturbance down to this optimal wall-normal position as it evolves over the interval. This effect is stronger for longer streamwise intervals where the suction will act on the disturbance over a longer distance. The vortex cores must therefore be located higher for a long interval than for a short in order for the disturbance to reach the optimal wall-normal coordinate at the end of the interval.

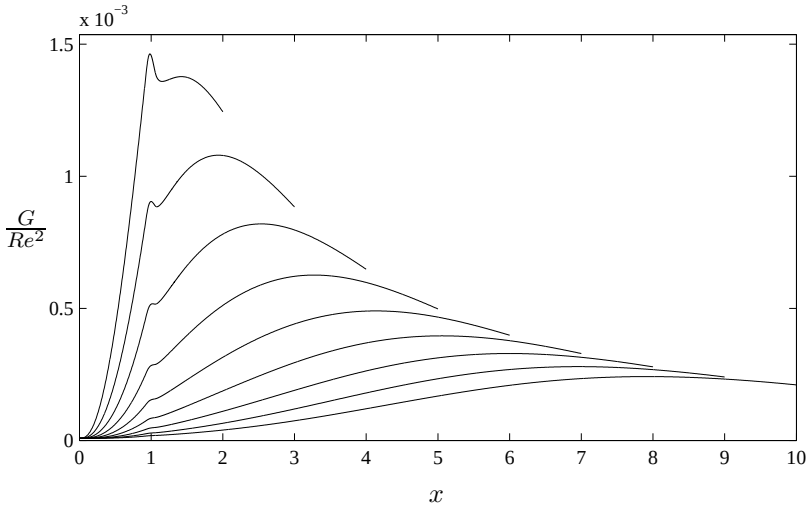

FIGURE 5. The growth G in the SSBL at $Re = 347$ as function of x for nine streamwise intervals ranging from $0 \leq x \leq 2$ to $0 \leq x \leq 10$ in steps of one. The optimal β of each respective interval was used, ω was set to zero.

3.2. *A comparison with the asymptotic suction boundary layer*

In this section we study the energy growth of the optimal disturbance in the ASBL and make a comparison between the SSBL and the ASBL. We study the ASBL over the same streamwise intervals that were used for the SSBL, although the suction is here applied over the whole interval. Since the base flow of the ASBL does not vary in the streamwise direction (see § 2), it is however arbitrary which interval we study as long as we keep the length constant. The Reynolds number Re was set to 347, as in the study of the SSBL.

The optimal disturbance in the ASBL takes the form of streamwise aligned vortex pairs that give rise to streamwise elongated streaks. This is in agreement with the results from the temporal study of the ASBL by Fransson & Corbett (2003). The dependence on the spanwise wavenumber β resembles that found for the SSBL (see table 2) and the optimal angular frequency ω was found to be zero irrespective of the interval length. Figure 8 shows the growth as function of the streamwise coordinate for all nine streamwise intervals, the optimal β for each respective interval was used in these calculations and ω was set to zero. For all the intervals the optimal growth is exceeded by maxima upstream of the endpoints. An optimization of the endpoint of the streamwise interval was therefore carried out, it was found that the largest possible growth of $G = 0.11 \cdot 10^{-2} Re^2$ occurs when $x_1 = 0.89$ and $\beta = 0.52$, the dashed line in figure 8. This result can be compared with the temporal study of the ASBL by Fransson

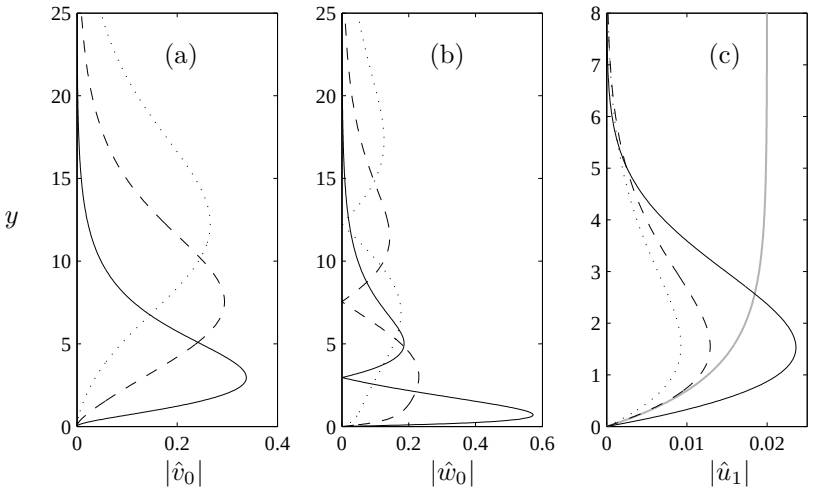

FIGURE 6. The optimal disturbance in the SSBL at $Re = 347$ and for the streamwise intervals $0 \leq x \leq 2$ (solid line), $0 \leq x \leq 6$ (dashed line) and $0 \leq x \leq 10$ (dotted line). (a–b) The wall-normal component $\hat{v}_0$ and the spanwise component $\hat{w}_0$ of the optimal disturbance. (c) The downstream response of the optimal disturbance, streamwise component $\hat{u}_1$. Observe that the scaling of $\hat{u}$ differs a factor Re from the scaling of $\hat{v}$ and $\hat{w}$, see § 2. The grey line shows the ASBL, scaled down to fit the figure. The ASBL has been reached (within graphical accuracy) at the end of the streamwise intervals examined here.

& Corbett (2003). They found that the optimal disturbance, with $\beta = 0.53$, gives rise to a growth of $G = 0.99 \cdot 10^{-3} Re^2$ over the optimal temporal interval. The spatial growth presented here is 16% higher than this temporal result. Biau & Bottaro (2004), who carried out a study on optimal disturbances in the plane Poiseuille flow, also found that spatial analysis gives higher growth than the temporal analysis. The plane Poiseuille flow was implemented herein and the growth calculated for the optimal wavenumber and interval given by Biau & Bottaro (2004). The result matched that of Biau & Bottaro (2004) and thus validated the used optimization procedure.

It is interesting to compare the optimal disturbance in the SSBL with that in the ASBL since it will expose how the differences in the base flow at the beginning of the interval affect the disturbance as it evolves downstream. One would expect that the differences between the disturbances will go towards zero as the streamwise interval is prolonged since the base flow of the SSBL approaches that of the ASBL.

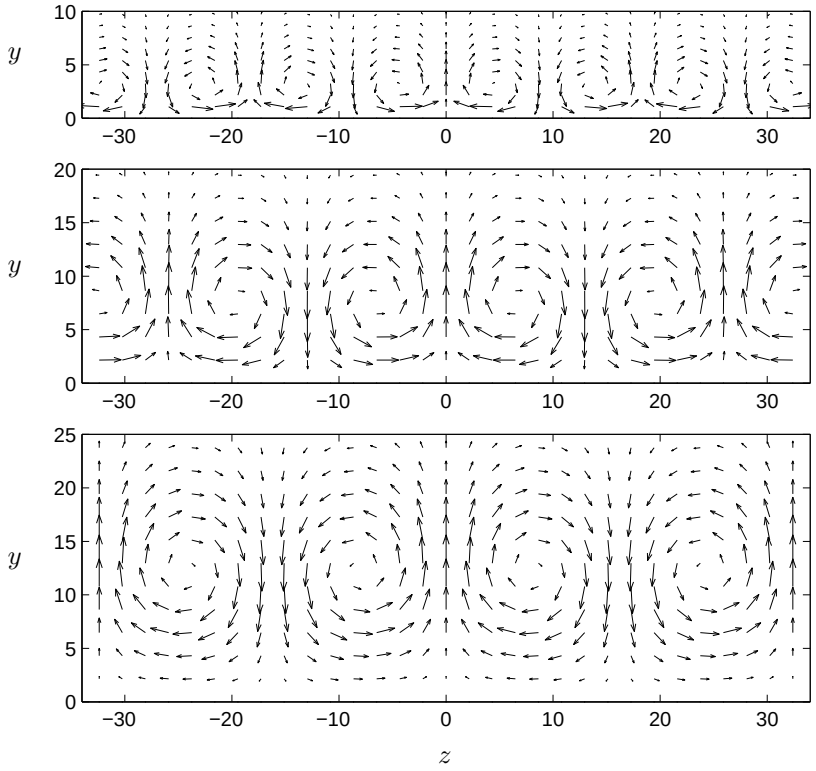

FIGURE 7. The optimal disturbance in the SSBL at $Re = 347$ for the streamwise intervals $0 \leq x \leq 2$ (upper row), $0 \leq x \leq 6$ (middle row) and $0 \leq x \leq 10$ (bottom row).

The left column of figure 9 shows the growth as function of the spanwise wavenumber β for both the SSBL (solid line) and the ASBL (dashed line) while the right column shows the growth as function of the streamwise coordinate x. The angular frequency ω was set to zero and the optimal β was used when the growth as function of x was calculated. Three different streamwise intervals were used, $0 \leq x \leq 2$, $0 \leq x \leq 6$ and $0 \leq x \leq 10$. For the shortest interval, shown in the upper row, the SSBL gives a 30% higher optimal growth than the ASBL. The optimal growth also occurs at a lower spanwise wavenumber for the SSBL than for the ASBL. Studying the growth as function of x, we gather that the reason for the large difference in growth is the contribution from the BBL at the beginning of the SSBL. The middle row shows the interval $0 \leq x \leq 6$, for this interval the curves lie much closer, but the SSBL still gives a slightly higher optimal growth than the ASBL. The optimal spanwise wavenumber is however the same. The contribution from the BBL is also much smaller, this

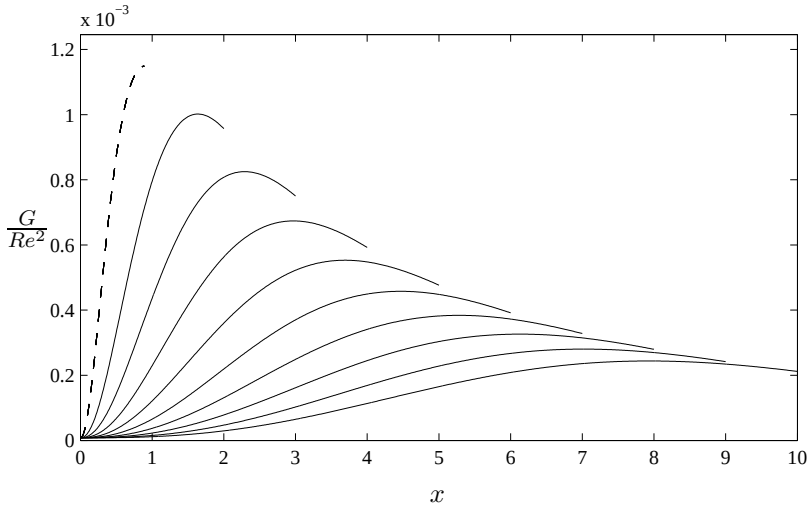

FIGURE 8. The growth G in the ASBL as function of x at $Re = 347$ for nine streamwise intervals ranging from $0 \leq x \leq 2$ to $0 \leq x \leq 10$ in steps of one (solid lines) and for the optimal interval $0 \leq x \leq 0.89$ (dashed line). The optimal β of each respective interval was used in these calculations and ω was set to zero.

explains why the optimal growth in the SSBL ends up so much closer to that in the ASBL. Finally we examine the long streamwise interval $0 \leq x \leq 10$, shown in the bottom row of figure 9. The curves collapse when we study the growth as function of the spanwise wavenumber, but a small difference can still be seen at the beginning of the streamwise interval. A more detailed comparison is done in table 2, which states the optimal spanwise wavenumber and corresponding optimal growth for all streamwise intervals. We conclude that the optimal growth and spanwise wavenumber in the SSBL go towards those in the ASBL when the streamwise interval is prolonged.

In figure 10 we compare the optimal disturbance in the SSBL (solid lines) and the ASBL (dashed lines). The upper row shows the wall-normal component $\hat{v}_0$ while the bottom row shows the spanwise component $\hat{w}_0$. The left, middle and right columns show the disturbances in the streamwise intervals $0 \leq x \leq 2$, $0 \leq x \leq 6$ and $0 \leq x \leq 10$, respectively. This figure reveals that there are significant differences between the optimal disturbance in the SSBL and the optimal disturbance in the ASBL. For the shortest streamwise interval, the shapes of the disturbance profiles differ, especially for the $\hat{w}$ component which is larger close to the wall in the SSBL than in the ASBL. For the longer intervals, the disturbances assume more or less the same shape, but the profile

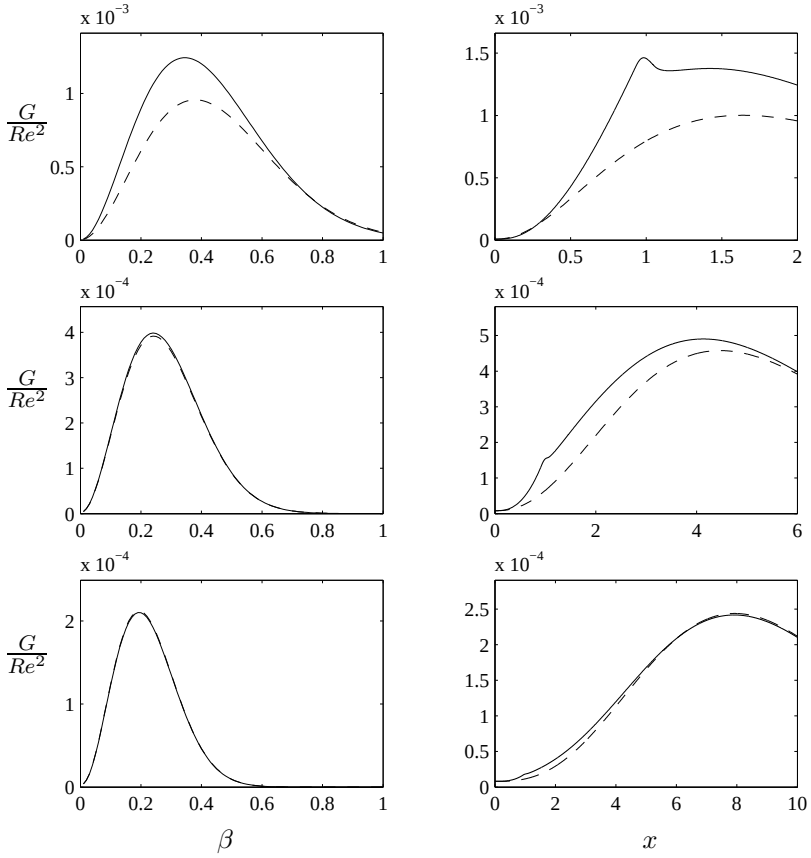

FIGURE 9. Left column: the growth G as function of β. Right column: the growth of the disturbance with optimal β as function of x. The SSBL (solid line) and the ASBL (dashed line) at $Re = 347$. The upper, middle and bottom row shows the growth in the streamwise intervals $0 \leq x \leq 2$, $0 \leq x \leq 6$ and $0 \leq x \leq 10$, respectively.

maxima are still located slightly higher in the ASBL than in the SSBL. This is due to the fact that the suction acts on the disturbance over a longer distance in the ASBL where the suction is applied over the whole interval. When the $\hat{v}$ and $\hat{w}$ components in the longest interval are plotted at $x = 1$ (not shown here), the disturbances in the ASBL and the SSBL almost collapse.

The optimal disturbance evolves downstream to the final position of the interval, shown in figure 11. The differences are now much smaller and only clearly visible for the shortest interval. There is no significant difference in

TABLE 2. The optimal growth and spanwise wavenumber in the ASBL and the SSBL at $Re = 347$ for nine streamwise intervals of different length.

x_1	2	3	4	5	6	7	8	9	10
β_{ASBL}	0.38	0.32	0.29	0.26	0.24	0.23	0.21	0.20	0.19
β_{SSBL}	0.35	0.31	0.28	0.26	0.24	0.23	0.21	0.20	0.19
$G_{\text{ASBL}}/Re^2 \cdot 10^2$	0.096	0.075	0.059	0.048	0.039	0.033	0.028	0.024	0.021
$G_{\text{SSBL}}/Re^2 \cdot 10^2$	0.12	0.088	0.065	0.050	0.040	0.033	0.028	0.024	0.021

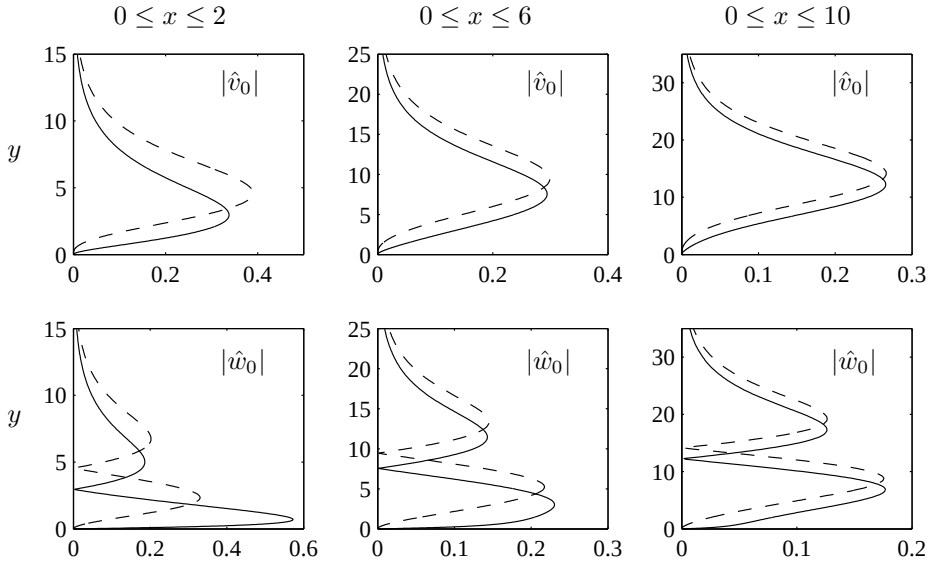

FIGURE 10. The optimal disturbance in the SSBL (solid line) and the ASBL (dashed line) at $Re = 347$. The upper and bottom row shows respectively the wall-normal component $\hat{v}_0$ and the spanwise component $\hat{w}_0$.

the wall-normal distribution or shape of the disturbances, we conclude that for long intervals the downstream response of the optimal disturbance in the SSBL and the ASBL have the same shape and wall-normal distribution.

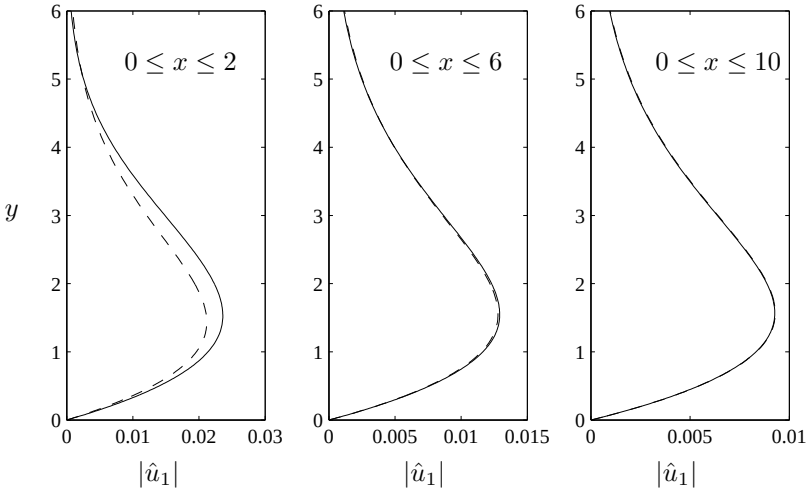

FIGURE 11. The downstream response $\hat{u}_1$ of the optimal disturbance in the SSBL (solid line) and the ASBL (dashed line) at $Re = 347$.

3.3. *Comparison with experimental results*

As previously mentioned, Fransson & Alfredsson (2003) made an experimental study on the development and growth of disturbances induced into the SSBL by free-stream turbulence. The suction Reynolds numbers was $Re = 347$ and the suction started 360mm downstream of the leading edge. Fransson & Alfredsson (2003) found that the spanwise wavenumber of the streaks depends on the level of the free-stream turbulence. Three grids were used to achieve different levels of turbulence; 1.4%, 2.2% and 4.0%. For these turbulence levels the measured spanwise wavenumbers were $\beta = 0.33$, $\beta = 0.41$ and $\beta = 0.47$, respectively. Fransson & Alfredsson (2003) furthermore report that the spanwise scale of the streaks is maintained when suction is applied compared with the no-suction case. According to Fransson & Alfredsson (2003), the initial spanwise scale is probably set by the receptivity process in the BBL at the leading edge of the SSBL. The optimal wavenumber in the ASBL is $\beta = 0.53$ (Fransson & Corbett (2003)) with temporal analysis and $\beta = 0.52$ with the spatial analysis presented herein. Fransson & Corbett (2003) argue that the experimentally measured spanwise wavenumber approaches the optimal wavenumber as the free-stream turbulence level is increased. Their reasoning is that a high level of free-stream turbulence will provide enough energy over the whole range of scales to allow the boundary layer to amplify the disturbance with a wavenumber close to that of the optimal disturbance. There is however a discrepancy between the optimal and the measured wavenumber, even for the highest turbulence level. Fransson & Corbett (2003) found good agreement between the downstream

response to the optimal disturbance and experimentally measured disturbance profiles (Fransson & Alfredsson (2003)). Equally good agreement was obtained with the present spatial analysis of the SSBL (not shown in figure).

In the present study the suction Reynolds number was set to $Re = 347$ and the suction was started at $x_s = 1$, emulating the base flow of the experiment by Fransson & Alfredsson (2003). In § 3.1b it was shown that in this base flow the optimal growth decays when the endpoint of the interval is moved downstream of the point where the suction starts. The growth in the downstream region can therefore never surpass that obtained over the BBL in the upstream region where no suction is applied. The following hypothesis could therefore provide an explanation to why Fransson & Alfredsson (2003) found that the spanwise scale of the streaks in the SSBL is close to the scale in the BBL. The free-stream turbulence contains a broad spectrum of spanwise scales, disturbances of scales close to the optimal scale in the BBL will experience the greatest growth and thus become dominating in the upstream region where no suction is applied. Other scales could however be present at the downstream position where the suction starts. It is possible that disturbances of different scales are continuously induced into the boundary layer downstream of the leading edge region, due to the forcing from the free-stream turbulence. Disturbances of scales close to the optimal in the ASBL should experience the greatest growth in the downstream region where suction is applied. There is however no possibility for these disturbances to grow and become dominating, since even disturbances of the optimal scale decay in the downstream region (§ 3.1b). The streaks which dominated in the upstream region will therefore continue to dominate in the downstream region. This could explain why the experimentally observed streaks in the SSBL are of almost the same spanwise scale as those dominating in the BBL. The fact that the optimal growth decays in the downstream region is due to the relatively high suction rate used in the present study. Calculations with the present implementation have however shown that the maximum energy growth can be located downstream of the point where the suction starts, if the suction rate is sufficiently low. These results are not included in the present study since our primary interest lies in emulating the base flow of the experiments by Fransson & Alfredsson (2003).

Yoshioka *et al.* (2004) extended the study of Fransson & Alfredsson (2003) to different turbulence levels, suction and free-stream velocities. For conditions close to those of the experiment by Fransson & Alfredsson (2003), Yoshioka *et al.* (2004) found that the disturbances are passively convected downstream without changing the spanwise scale. By simultaneously changing the suction and free-stream velocity, the suction Reynolds number was kept constant while the displacement thickness in the ASBL region was increased, thereby decreasing the difference in displacement thickness between the BBL upstream and the ASBL downstream. For these conditions, Yoshioka *et al.* (2004) argue that the scale of the streaks approach the temporal optimal scale in the ASBL. In

the current study it has been shown (table 2) that the spanwise scale of the optimal disturbance in the ASBL depends on the streamwise interval length. Although the optimal scale in the optimal interval ($0 \leq x \leq 0.89$) is nearly identical to that found with temporal analysis (Fransson & Corbett (2003)), it is significantly wider in longer intervals.

To summarize, the experimental findings show that the spanwise scale of the streaks in the SSBL is close to the scale of the streaks in the BBL where no suction is applied. A possible explanation is provided in the current study, which shows that the relatively high suction rate makes it impossible for disturbances of the optimal scale in the ASBL to grow in the downstream region affected by suction. This region will therefore be dominated by streaks of scales close to the optimal scale in the BBL, since these disturbances have already grown to large amplitudes in the upstream region unaffected by suction. There are however important differences between the calculation of optimal disturbances presented herein and the experimental conditions. In the calculation of the optimal disturbance we assume that the disturbance enter the boundary layer at the initial point of the streamwise interval and then evolves downstream without any influence from the outside disturbance environment. In the experiment the boundary layer is subjected to continuous forcing from the free-stream turbulence over the entire streamwise interval. It is also possible that nonlinear effects that are not accounted for in the calculation of the optimal disturbances occur in the experiment.

4. Conclusions

The energy growth of optimal disturbances was studied by means of linearized equations for the semi suction boundary layer (SSBL) and the asymptotic suction boundary layer (ASBL). The suction Reynolds number was set to 347.

Firstly, the algebraic growth in the SSBL was studied. It was found that the optimal disturbance consists of streamwise aligned vortex pairs that give rise to streamwise streaks. This disturbance gives rise to the highest possible growth when the streamwise interval ends at the point where the suction starts. The base flow of this optimal interval is the BBL, the optimal spanwise wavenumber in the SSBL is therefore the same as that in the BBL, $\beta = 0.45$ (Andersson *et al.* (1999); Luchini (2000)). When the interval is prolonged beyond the starting point of the suction, the optimal spanwise wavenumber decreases, the optimal angular frequency is however zero irrespective of the interval length. Furthermore, it was found that the vortices, i.e. the optimal disturbance, grow as the interval is prolonged and that the cores of the vortices move upward in the wall-normal direction. This effect is due to the suction which draws the disturbance down towards the wall. The vortex cores must therefore be located higher initially in a long interval where the suction will act on the disturbance over a longer distance.

Secondly, the optimal disturbance in the ASBL was studied and a comparison with the SSBL was made. The optimal disturbance in the ASBL closely resembles that in the SSBL. The cores of the vortices, i.e. the optimal disturbance, are however located higher in the ASBL due to the fact that the suction acts on the disturbance over the whole streamwise interval. This difference vanishes as the disturbance evolves in the streamwise direction, the downstream response is therefore the same over long intervals. Furthermore, it was found that for short intervals the SSBL gives a significantly higher growth due to the contribution from the BBL. The optimal spanwise wavenumber was also lower for the SSBL than for the ASBL for these intervals. As the streamwise interval was prolonged the optimal growth and spanwise wavenumber in the SSBL approached those in the ASBL.

Finally, a comparison was made with experimental results from Fransson & Alfredsson (2003) and Yoshioka *et al.* (2004). This comparison showed that both the experimental findings and the results presented herein support the theory that the spanwise scale of the disturbances is set in the BBL at the leading edge of the SSBL.

Acknowledgements

The authors thank Doctor J. H. M. Fransson who provided many insightful comments, from which this work has greatly benefitted. We are indebted to Doctor P. Corbett, Professor A. Bottaro and Doctor J. H. M. Fransson who generously shared their code for temporal analysis of optimal disturbances.

References

Andersson, P., Berggren, M. & Henningson, D. 1999 Optimal disturbances and bypass transition in boundary layers. *Phys. Fluids* **11** (1), 134–150.

Andersson, P., Brandt, L., Bottaro, A. & Henningson, D. S. 2001 On the breakdown of boundary layer streaks. *J. Fluid Mech.* **428**, 29–60.

Balakumar, P. & Hall, P. 1999 Optimum suction distribution for transition control. *Theoret. Comput. Fluid Dyn.* **13**, 1–19.

Berlin, S. & Henningson, D. S. 1996 A nonlinear mechanism for receptivity of free-stream disturbances. *Phys. Fluids* **11** (12), 3749–3760.

Biau, D. & Bottaro, A. 2004 Transient growth and minimal defects: Two possible initial paths of transition to turbulence in plane shear flows. *Phys. Fluids* **16** (10), 3515–3529.

Brandt, L. & Henningson, D. S. 2002 Transition of streamwise streaks in zero-pressure-gradient boundary layers. *J. Fluid Mech.* **472**, 229–261.

Butler, K. M. & Farrell, V. F. 1992 Three-dimensional optimal perturbations in viscous shear flow. *Phys. Fluids A* **4** (8), 1637–1650.

Corbett, P. & Bottaro, A. 2000 Optimal perturbations for boundary layers subject to stream-wise pressure gradient. *Phys. Fluids* **12** (1), 120–130.

Corbett, P. & Bottaro, A. 2001 Optimal linear growth in swept boundary layers. *J. Fluid Mech.* **435**, 1–23.

Corbett, P. & Bottaro, A. 2001 Optimal control of nonmodal disturbances in boundary layers. *Theoret. Comput. Fluid Dynamics* **15**, 65–81.

Ellingsen, T. & Palm, E. 1975 Stability of linear flow. *Phys. Fluids* **18** (4), 487–488.

Fransson, J. H. M. & Alfredsson, P. H. 2003 On the disturbance growth in an asymptotic suction boundary layer. *J. Fluid Mech.* **482**, 51–90.

Fransson, J. H. M. & Corbett, P. 2003 Optimal linear growth in the asymptotic suction boundary layer. *Eur. J. Mech., B/Fluids* **22**, 259–270.

Fransson, J. H. M., Matsubara, M. & Alfredsson, P. H. 2005 Transition induced by free-stream turbulence. *J. Fluid Mech.* **527**, 1–25.

Griffith, A. A. & Meredith, F. W. 1936 The possible improvement in aircraft performance due to boundary layer suction. Tech. Rep. 2315, Rep. Aero. Res. Coun. (1936).

Hœpffner, J., Brandt, L. & Henningson, D. S. 2005 Transient growth on boundary layer streaks. *J. Fluid Mech.* **537**, 91–100.

Klebanoff, P. S. 1971 Effect of freestream turbulence on the laminar boundary layer. *Bull. Am. Phys. Soc.* **10**, 1323.

Landahl, M. T. 1975 Wave breakdown and turbulence. *SIAM J. Appl. Maths* **28** (4), 735–756.

Landahl, M. T. 1980 A note on an algebraic instability of inviscid parallel shear flows. *J. Fluid Mech.* **98** (2), 243–251.

Levin, O. & Henningson, D. S. 2003 Exponential vs algebraic growth and transition prediction in boundary layer flow. *Flow, Turbulence and Combustion* **70**, 183–210.

Luchini, P. 2000 Reynolds-number-independent instability of the boundary layer over a flat surface: optimal perturbations. *J. Fluid Mech.* **404**, 289–309.

Matsubara, M. & Alfredsson, P. H. 2001 Disturbance growth in boundary layers subjected to free-stream turbulence. *J. Fluid Mech.* **430**, 149–168.

Pralits, J. O., Hanifi, A. & Henningson, D. S. 2002 Adjoint-based optimization of steady suction for disturbance control in incompressible flows. *J. Fluid Mech.* **467**, 129–161.

Reddy, S. C. & Henningson, D. S. 1993 Energy growth in viscous channel flows. *J. Fluid Mech.* **252**, 209–238.

Schlichting, H. 1979 Boundary-Layer Theory, 7th Edition, Mc-GRAW HILL

Schmid, P. J. & Henningson, D. S. 2001 Stability and transition in shear flows, Springer.

Westin, K. J. A., Boiko, A. V., Klingmann, B. G. B., Kozlov, V. V. & Alfredsson, P. H. 1995 Experiments in a boundary layer subjected to free stream turbulence. Part 1. Boundary layer structure and receptivity. *J. Fluid Mech.* **281**, 193–218.

Yoshioka, S., Fransson, J. H. M. & Alfredsson, P. H. 2004 Free stream turbulence induced disturbances in boundary layers with wall suction. *Phys. Fluids* **16** (11), 3530–3539.

Zuccher, S., Luchini, P. & Bottaro, A. 2004 Algebraic growth in a Blasius boundary layer: optimal and robust control by mean suction in the nonlinear regime. *J. Fluid Mech.* **513**, 135–160.

2

Paper 2

Optimal disturbances in the Falkner–Skan–Cooke boundary layer

By Martin G. Byström, Ardeshir Hanifi and Dan S. Henningson

The algebraic growth of spanwise periodic, stationary disturbances is studied in the sub-critical Falkner–Skan–Cooke boundary layer. An adjoint-based optimization procedure is used to find the initial disturbances associated with the maximum energy growth. It is shown that these optimal disturbances take the form of tilted vortices in the cross-flow plane. The vortices give rise to tilted streaks of alternating high and low streamwise velocity. Secondly, the streamwise interval was extended to include the super-critical part of the boundary layer. As the disturbances evolve downstream into this region, the algebraic growth growth pass over to exponential amplification. A comparison to calculations with parabolized stability equations shows that the disturbances evolve into cross-flow modes in the super-critical flow. The disturbance shape does not undergo any dramatic changes as the disturbances evolve from the sub-critical to the super-critical flow. It is therefore concluded that similar physical mechanisms drive both the algebraic and the exponential instability.

1. Introduction

Ellingsen & Palm (1975) showed that three-dimensional (3D) disturbances can attain linear growth over time in inviscid channel flow, even when the flow does not posses any inflection point and thus is stable according to classical eigenvalue analysis. The inviscid, algebraic growth will eventually die out exponentially through viscous dissipation, as concluded by Hultgren & Gustavsson (1981). This instability is therefore denoted algebraic or transient growth. Landahl (1975,1980) illuminated the physical mechanism behind transient growth, arguing that when a fluid element is lifted up in the wall-normal direction it will initially maintain its horizontal momentum. Hence, small perturbations in the wall-normal direction can cause large disturbances in the streamwise direction. This mechanism, commonly referred to as the *lift-up* effect, is responsible for the formation of streamwise streaks in boundary layers subjected to vortical disturbances such as free-stream turbulence. Such disturbances are also known as Klebanoff modes, after the experimental study by Klebanoff (1971). Since then, this type of disturbances have been studied in a number of experiments,

see e.g. Matsubara & Alfredsson (2001). From a mathematical viewpoint, the transient growth is due to the non-orthogonality of the governing equations, as outlined in Trefethen *et al.* (1993). Butler & Farrell (1992), Henningson *et al.* (1993) and Reddy & Henningson (1993) computed the disturbances associated with the maximum transient growth in various parallel flows by optimizing over the eigenmodes of the Orr–Sommerfeld operator. Hanifi *et al.* (1996) extended this methology to compressible flow. Luchini (1996) studied 3D, spanwise periodic disturbances in the Blasius boundary layer. He concluded that a mode with unbounded growth exists in the spatially broadening boundary layer, where the effect of viscosity weakens with distance. The study was however restricted to small spanwise wavenumbers, making it impossible to determine the wavenumber associated with maximum energy growth. This wavenumber was later determined by Andersson *et al.* (1999) and Luchini (2000), who independently used adjoint-based optimization to identify the initial disturbance associated with maximum energy growth in the developing Blasius boundary layer. As in previous studies, it was found that these disturbances take form of streamwise oriented vortices which give rise to streamwise streaks through the lift-up effect. Tumin & Reshotko (2003) expanded the spatial analysis to the developing, compressible boundary layer.

The spatial analysis of transient growth has so far been restricted to two-dimensional (2D) boundary layers. For such flows it can be stated that the disturbances responsible for maximum algebraic growth bears little resemblance to the instabilities predicted by classical eigenvalue analysis, i.e. Tollmien–Schlichting waves (TS-waves). The former has the form of stationary streamwise aligned vortices which gives raise to infinitely elongated streamwise streaks with short spanwise wavelength, while the latter consists of travelling waves with short wavelength in the streamwise direction and long wavelengths with respect to the spanwise axis. The 2D boundary layer can thus be considered a scene where algebraic and exponential instability constitutes two different, competing physical mechanisms. Which type of instability that causes the transition to turbulence is largely down to the external forcing which the boundary layer is subjected to. The situation is different in the swept boundary layers, where stationary unstable eigenmodes exists. These modal instabilities take the form of vortices, nearly aligned with the external streamline, and elongated streamwise streaks. The exponentially growing eigenmodes of the 3D boundary layer thus resembles the algebraically growing, non-modal disturbances of the 2D boundary layer. The question therefore arises, whether algebraic and exponential growth may be driven by the same physical mechanism in 3D boundary layers.

Corbett & Bottaro (2001) utilized temporal analysis to study transient growth in the Falkner–Skan–Cooke boundary layer, and employed an adjoint-based optimization procedure to determine the optimal initial disturbance which produces the greatest energy gain over a given time interval. It was

found that these optimal disturbances take the form of vortices nearly aligned with the external streamline, which over time give rise to streamwise streaks. Sub- and super-critical Reynolds numbers were considered and algebraically growing disturbances were compared to exponentially amplified eigenmodes. It was found that these two types of disturbances are similar, Corbett & Bottaro (2001) concluded that in swept flows the algebraic growth may precondition the boundary layer to exponential instabilities, i.e. the algebraically growing disturbances are fed into cross-flow eigenmodes as the critical Reynolds number is exceeded. The temporal analysis employed by Corbett & Bottaro (2001) does however not allow a study where the downstream development of the disturbances can be monitored as they evolve from the sub- to the super-critical domain of the boundary layer. Herein we will employ spatial analysis to perform such a study, presented in § 5.4.

Further motivation for studies of algebraic growth in swept boundary layers comes from the widespread appearance of such flows within aeronautical applications. Traditionally, the design of air-plane wings have often been aimed at prolonging the upstream region of accelerated flow, in order to delay the growth of TS-waves. A strong favorable pressure gradient will however also create a flow prone to cross-flow instability. The low-turbulence environment encountered at free-flight conditions is unlikely to trigger traveling disturbances. Stationary disturbances can however be initiated by sub-micron roughness on the wing surface, as described in Radeztsky *et al.* (1999).

Herein we will study stationary, spanwise periodic disturbances with infinite wavelength along the propagation direction in the Falkner–Skan–Cooke boundary layer. These disturbances experience algebraic growth in sub-critical flows, and exponential growth as they evolve downstream, into the super-critical domain of the boundary layer. The focus on stationary disturbances is motivated by the fact they are the most likely to cause transition, as discussed above. In § 3 we will introduce a parabolic set of equations which governs these disturbances. An adjoint-based optimization procedure is employed to identify the initial disturbances associated with the maximum energy growth, as described in § 4. In § 5.3 we will show that these optimal disturbances take the form of vortices, nearly aligned with the external streamline, which give rise to streamwise streaks. The growth of these disturbances change from algebraic to exponential when the chordwise interval is extended to include the super-critical part of the boundary layer. In § 5.4 it is shown that the resulting disturbances are identical to modal disturbances calculated with parabolized stability equations (PSE) in the super-critical region.

2. The Falkner–Skan–Cooke boundary layer

In the present report we will study the growth of small disturbances in a developing boundary layer over a swept, flat plate of infinite span, where a pressure

gradient is present in the chordwise direction. The scene of the survey is illustrated in figure 1, which also presents the utilized reference systems. Their definitions are as follows: i) Cartesian coordinate system aligned with the plate, denoted by x, where x^1, x^2 and x^3 are the axes in, respectively, the chordwise, the spanwise and the wall-normal directions. The corresponding velocity components are denoted U, V and W, respectively. ii) Cartesian coordinate system aligned with incoming flow, denoted by r. iii) Curvilinear, orthogonal coordinate system aligned with the external streamline, denoted by s. The axes s^1 and s^2 are, respectively, parallel and perpendicular to the streamline, and s^3 is normal to the plate. Hereafter, we will refer to these as the streamwise, cross-stream and wall-normal axes. The corresponding velocities will be denoted U_s, V_s and W_s, respectively. iiii) Non-orthogonal, curvilinear coordinate system which is utilized in the computations, as outlined in § 3. The coordinate axes ξ^1, ξ^2 and ξ^3 are, respectively, aligned with the streamline, parallel to the leading edge and normal to the plate. It can be noted that the wall-normal axis has the same direction in all four coordinate systems.

Our study will be restricted to flows with a fixed chordwise pressure gradient where the chordwise velocity at the boundary layer edge (superscript e) is given by a simple expression,

$$U^e = C\left(x^1\right)^m, \tag{1}$$

where $m = \beta_\mathrm{H}/\left(2-\beta_\mathrm{H}\right)$ and β_H is the Hartree parameter. Furthermore, it follows from the infinite span approximation that the spanwise component V^e is constant in the chordwise direction and that the flow is independent of the spanwise coordinate. For such simple 3D flows, often referred to as 2.5D, a family of similarity solutions exists for incompressible flows. The 2D Falkner–Skan similarity solutions (see e.g. Schlichting (1979)) were first extended to 2.5D boundary layers by Cooke (1950), as outlined in Corbett & Bottaro (2001). They are therefore named the Falkner–Skan–Cooke similarity solutions.

Although the present study is carried out for flows correctly described by the Falkner–Skan–Cooke similarity solutions, the meanflow was obtained by solving the compressible boundary layer equations. The motivation is that the present implementation will be utilized in future studies where the effect of compressibility, surface curvature and non-constant pressure gradients will be accounted for.

Figure 2 presents the streamwise and cross-flow velocity profiles, which are obtained from the cartesian velocity components by the following relations

$$U_\mathrm{s} = U\cos\Phi + V\sin\Phi, \tag{2}$$

$$V_\mathrm{s} = -U\sin\Phi + V\cos\Phi. \tag{3}$$

where Φ denotes the *streamline angle*, defined as $\Phi = \arctan\left(V^e/U^e\right)$.

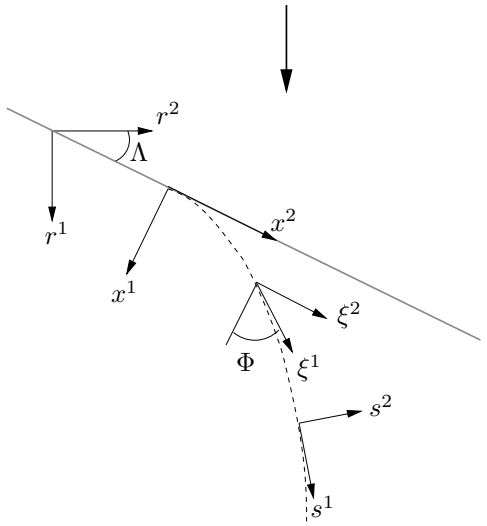

FIGURE 1. Flow over an infinite, flat plate with a sweep angle Λ. The *streamline angle*, i.e. the local angle between the external streamline (dashed line) and the chordwise axis (x^1), is denoted Φ. The four coordinate systems, denoted by r, x, ξ and s, are defined in § 2.

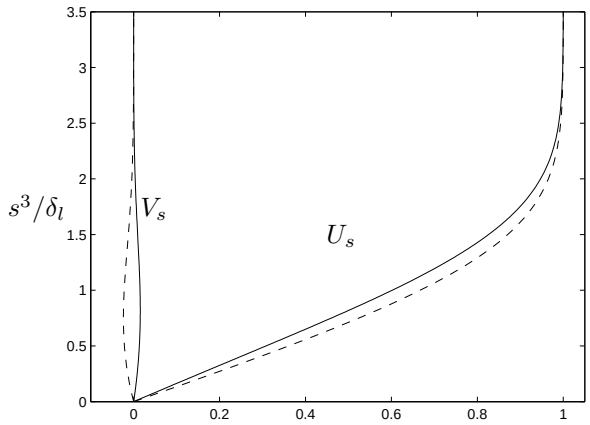

FIGURE 2. Profiles of the streamwise (U_s) and the cross-flow (V_s) velocity components in the Falkner–Skan–Cooke boundary layers with a sweep angle of $\Lambda = 45°$. Favorable and adverse pressure gradients of, respectively, $\beta_H = 0.1$ (dashed line) and $\beta_H = -0.05$ (solid line).

The relatively weak pressure gradients studied herein introduce cross-flow components which are small compared to the streamwise velocity. Furthermore it can be noted that the cross-flow component changes sign with β_H. As outlined in § 5.3, this has a bearing on the shape of the optimal disturbance.

In this report we will restrict our studies to boundary layers within the Falkner–Skan–Cooke family with a sweepangle of $\Lambda = 45°$. We consider both an accelerated flow with a chordwise pressure gradient of $\beta_{\mathrm{H}} = 0.1$ and a retarded flow; $\beta_{\mathrm{H}} = -0.05$. The chordwise velocity at the boundary layer edge (1) is chosen such that $\Phi = \Lambda = 45°$ at the chordwise position $r^1/l = 1$, where $R_l = U_l l/\nu = 10^6$ and $U_l = U_s\left(r^1 = l, r^3 = r^3_{\max}\right)$. We will employ two reference lengths for the presented figures, l and $\delta_l = \sqrt{\nu l/U_l}$.

3. Disturbance equations

In this section we will discuss the appropriate scaling, coordinate system and disturbance equations for our studies of transient growth in the Falkner–Skan–Cooke boundary layer. Herein, R denotes the Reynolds number $R = U_0\delta_0/\nu$ where U_0 is the chordwise velocity of the external flow at $x^1 = x^1_0$ and $\delta_0 = \sqrt{\nu x^1_0/U_0}$. Andersson *et al.* (1999) and Luchini (2000) employed the linearized disturbed boundary layer equations (LDBLE) in their independent studies of transient growth in the Blasius boundary layer. This analysis was later extended to the Falkner–Skan boundary layer by Levin & Henningson (2003), who presented a comparative study of algebraically growing streaks, governed by the LDBLE, and exponentially growing TS-waves governed by the PSE. Both set of equations are derived from the linearized Navier–Stokes equations, with the disturbance $\tilde{q}$ assumed to be of the form

$$\tilde{q}\left(x^1, x^2, x^3, t\right) \;=\; \hat{q}\left(x^1, x^3\right) \exp\left[i\left(\int \alpha \,\mathrm{d}x^1 + \beta x^2 - \omega t\right)\right]. \qquad (4)$$

where $\hat{q}$ is a complex amplitude function, α and β are the chordwise and spanwise wavenumbers, respectively, and ω is the angular frequency. The principal difference is that the PSE accounts for disturbances with a rapid, oscillatory variation in the chordwise direction while the LDBLE assumes a slow, non-oscillatory variation, hence the chordwise wavenumber is zero. Due to the different choices of scaling, the LDBLE is a Reynolds-number independent set of equations, identical to the Görtler equations with zero Görtler number (see Floryan & Saric (1979) and Hall (1983)), while the PSE are Reynolds-number dependent.

In his study of transient growth in the Blasius boundary layer, Luchini (2000) noted that the region of maximum algebraic instability, at zero frequency, is well separated from the region of the classical exponential instability in the frequency-Reynolds-number plane. In 3D boundary layers, where stationary cross-flow modes receive exponential amplification, no such separation exists. We can therefore expect a scenario where algebraic growth at

sub-critical Reynolds-numbers is followed by exponential amplification further downstream. It is clear that the spatial analysis of transient growth in 2D boundary layers cannot readily be extended to 3D flows. There are principal differences that need to be taken under consideration: i) Contrary to studies of algebraic growth in 2D boundary layers, the 2.5D problem is not Reynolds-number independent. That is, at some downstream position the neutral stability point for stationary modal disturbances will be passed and the algebraic growth will pass over to exponential amplification. The valid disturbance equations must therefore be Reynolds-number dependent. ii) The boundary layer scaling employed by Andersson *et al.* (1999) and Luchini (2000), where the spanwise component is considered an order lower than the chordwise component, is not valid for 2.5D boundary layers at high sweepangles. iii) The chordwise wavenumber α can not be set to zero in the 2.5D flow, since the disturbances are not aligned with this axis.

The PSE has successfully been employed in studies of stationary cross-flow modes, see e.g. the comparison with DNS results in Högberg & Henningson (1998). According to Corbett & Bottaro (2001), the physical mechanism behind transient growth in the Falkner–Skan–Cooke boundary layer is similar to that of the exponentially amplified cross-flow modes. Bagheri & Hanifi (2007) (paper + private communication) modified the PSE to obtain a parabolic set of equations, which was employed to calculate the algebraic growth of longitudinal vortices. They considered disturbances with infinite chordwise wavelength and kept $\mathcal{O}\left(R^{-2}\right)$ terms, namely $W_{x^1}\hat{u}$ (W and $\hat{u}$ are the wall-normal and chordwise components of the meanflow and the disturbance, respectively) in the wall-normal momentum equation. Calculations showed that this term has a significant impact on algebraic instabilities but no bearing on the exponentially growing TS-waves. Furthermore, Bagheri (2006) omitted the chordwise gradient of the disturbance pressure, $\hat{p}_{x^1}$, from the chordwise momentum equation. This term, associated with rapid oscillations in time, is neglectable for the stationary disturbances associated with the maximum algebraic growth. The calculated energy growth agreed very well with that reported by Levin & Henningson (2003).

Herein we will employ a similar set of parabolic equations to study transient growth in the Falkner–Skan–Cooke boundary layer. In order to do so, we must however first find an integration path along which the wavenumber can be set to zero. It is well known that disturbances tend to be aligned with the external streamline in 3D boundary layers, i.e. the streamwise wavenumber is zero. We will therefore formulate the disturbance equations for the non-orthogonal coordinate system ξ where the first axis ξ^1 is aligned with the external streamline. From the geometry given by figure 1, the following relationships between the cartesian and the non-orthogonal, curvilinear coordinate systems can be established,

$$\mathrm{d}x^1 \;=\; \cos\left(\Phi\left(\xi^1\right)\right)\,\mathrm{d}\xi^1, \quad \mathrm{d}x^2 \;=\; \mathrm{d}\xi^2 + \sin\left(\Phi\left(\xi^1\right)\right)\,\mathrm{d}\xi^1, \quad \mathrm{d}x^3 \;=\; \mathrm{d}\xi^3. \tag{5}$$

Jacobian transformation was herein employed to define the partial derivatives of the cartesian coordinates with respect to the non-orthogonal coordinates. From the relations above, the following operators can be defined

$$\nabla\,\psi \;=\; \left[\frac{\partial\psi}{\partial x^1},\,\frac{\partial\psi}{\partial x^2},\,\frac{\partial\psi}{\partial x^3}\right] \;=\; \left[\tilde{c}\frac{\partial\psi}{\partial\xi^1} - \tilde{t}\,\frac{\partial\psi}{\partial\xi^2},\,\frac{\partial\psi}{\partial\xi^2},\,\frac{\partial\psi}{\partial\xi^3}\right] \tag{6}$$

$$\nabla\cdot\vec{\boldsymbol{F}} \;=\; \frac{\partial F_1}{\partial x^1} + \frac{\partial F_2}{\partial x^2} + \frac{\partial F_3}{\partial x^3} \;=\; \tilde{c}\frac{\partial F^1}{\partial\xi^1} - \tilde{t}\,\frac{\partial F^1}{\partial\xi^2} + \frac{\partial F^2}{\partial\xi^2} + \frac{\partial F^3}{\partial\xi^3} \tag{7}$$

$$\nabla\times\vec{\boldsymbol{F}} = \left[\frac{\partial F^3}{\partial x^2} - \frac{\partial F^2}{\partial x^3},\,\frac{\partial F^1}{\partial x^3} - \frac{\partial F^3}{\partial x^1},\,\frac{\partial F^2}{\partial x^1} - \frac{\partial F^1}{\partial x^2}\right] \;= \tag{8}$$

$$\left[\frac{\partial F^3}{\partial\xi^2} - \frac{\partial F^2}{\partial\xi^3},\,\frac{\partial F^1}{\partial\xi^3} - \tilde{c}\frac{\partial F^3}{\partial\xi^1} + \tilde{t}\,\frac{\partial F^3}{\partial\xi^2},\,\tilde{c}\frac{\partial F^2}{\partial\xi^1} + \tilde{t}\,\frac{\partial F^2}{\partial\xi^2} - \frac{\partial F^1}{\partial\xi^2}\right]$$

where $\tilde{c} = 1/\cos(\Phi)$, $\tilde{t} = \tan(\Phi)$, and ψ and $\vec{F}$ denotes, respectively, an arbitrary scalar and vector function. Note that from these operators the Laplacian can be defined as

$$\nabla^2\vec{\boldsymbol{F}} = \nabla\left(\nabla\cdot\vec{\boldsymbol{F}}\right) - \nabla\times\left(\nabla\times\vec{\boldsymbol{F}}\right) \tag{9}$$

The conservation of mass, momentum and energy and the equation of state serves as the governing equations for the flow of a viscous, compressible, ideal gas. Expressed in primitive variables, these equations can be written in vector notation as

$$\rho\,[\frac{\partial\mathbf{u}}{\partial t} + (\mathbf{u}\cdot\nabla)\mathbf{u}] = -\nabla p + \frac{1}{R}\nabla[\lambda(\nabla\cdot\mathbf{u})] + \frac{1}{R}\nabla\cdot[\mu(\nabla\mathbf{u} + \nabla\mathbf{u}^T)], \tag{10}$$

$$\frac{\partial\rho}{\partial t} + \nabla\cdot(\rho\mathbf{u}) = 0, \tag{11}$$

$$\rho c_p[\frac{\partial T}{\partial t} + (\mathbf{u}\cdot\nabla)T] = \frac{1}{R\mathrm{Pr}}\nabla\cdot(\kappa\nabla T) + (\gamma-1)M^2[\frac{\partial p}{\partial t} + (\mathbf{u}\cdot\nabla)p + \frac{1}{R}\Phi], \tag{12}$$

$$\gamma M^2 p = \rho T, \tag{13}$$

with viscous dissipation given as

$$\Phi = \lambda(\nabla\cdot\mathbf{u})^2 + \frac{1}{2}\mu[\nabla\mathbf{u} + \nabla\mathbf{u}^T] : [\nabla\mathbf{u} + \nabla\mathbf{u}^T]$$

where $A : B = A_{ij}B_{ij}$. Here t represents time, ρ, p, T stand for density, pressure and temperature, $\mathbf{u}$ is the velocity vector. The Mach-number is denoted M and the Prandtl-number Pr. The quantities λ, μ stand for the second and dynamic viscosity coefficient, γ is the ratio of specific heats, κ the heat conductivity, c_p the specific heat at constant pressure. All flow quantities are made non-dimensional by the corresponding reference flow quantities at the chordwise position x_0^1, except the pressure which is referred to twice the corresponding

dynamic pressure. The reference length is $\delta_0 = \sqrt{\nu x_0^1/U_0}$. Using the operators (6-9), the partial derivatives of the equations are rewritten from the cartesian coordinate system to the non-orthogonal, curvilinear coordinate system. Note that we keep the cartesian velocity components in the equations. The flow and material quantities are decomposed into a mean part and a disturbance $\tilde{q} = [\tilde{u}, \tilde{v}, \tilde{w}, \tilde{p}, \tilde{T}, \tilde{\rho}]$, where u, v, w are the cartesian velocity components in the chordwise, spanwise and wall-normal direction, respectively. Under the infinite span approximation the mean flow is considered to be independent of the spanwise coordinate ξ^2. By subtracting the equations for the mean flow and removing the products of disturbances, a linearized set of disturbance equations is obtained. The disturbances are assumed to be spanwise periodic and non-oscillatory in the streamwise direction, hence the streamwise wavenumber is set to zero. Herein we will only consider stationary disturbances, the total disturbance (4) can thus be simplified to

$$\tilde{q}\left(\xi^1, \xi^2, \xi^3\right) \;=\; \hat{q}(\xi^1, \xi^3) \exp\left(i\beta\xi^2\right). \tag{14}$$

Furthermore it is assumed that the variation along the streamline is weak, i.e. $\partial/\partial\xi^1 \sim \mathcal{O}\left(R^{-1}\right)$. Note that here we modify the PSE by assuming that W is of the same order as the other velocity components of the meanflow. Introducing the disturbance (14) into the linearized equations and dropping terms associated with the streamwise pressure gradient yields a parabolic set of disturbance equations:

$$\boldsymbol{A}\hat{\boldsymbol{\phi}} + \boldsymbol{B}\frac{\partial\hat{\boldsymbol{\phi}}}{\partial\xi^3} + \boldsymbol{C}\frac{\partial^2\hat{\boldsymbol{\phi}}}{\partial\xi^3\partial\xi^3} + \boldsymbol{D}\frac{\partial\hat{\boldsymbol{\phi}}}{\partial\xi^1} \;=\; \boldsymbol{0}, \tag{15}$$

where $\hat{\boldsymbol{\phi}} = (\hat{\rho}, \hat{u}, \hat{v}, \hat{w}, \hat{T})^{\mathrm{T}}$. Note that the equation of state has been employed to express the disturbance pressure as a function of the density and temperature, the system is thus reduced to five equations. The elements of the matrices $\boldsymbol{A}$, $\boldsymbol{B}$, $\boldsymbol{C}$, $\boldsymbol{D}$ are given in appendix B.

The velocity disturbances are subjected to no-slip boundary conditions and vanishing in the free-stream, the same conditions are applied to the disturbance temperature

$$\hat{u} = \hat{v} = \hat{w} = \hat{T} = 0 \quad \text{at} \quad \xi^3 = 0 \tag{16}$$

$$\hat{u} = \hat{v} = \hat{w} = \hat{T} = 0 \quad \text{at} \quad \xi^3 = \xi^3_{\max} \tag{17}$$

Furthermore, the initial conditions must be specified at the inlet:

$$\hat{\boldsymbol{\phi}}\left(\xi^1 = 0, \xi^3\right) = \hat{\boldsymbol{\phi}}_{\mathrm{in}}\left(\xi^3\right) \tag{18}$$

where $\boldsymbol{\phi}_{\mathrm{in}} = [\rho_{\mathrm{in}}, u_{\mathrm{in}}, v_{\mathrm{in}}, w_{\mathrm{in}}, T_{\mathrm{in}}]^{\mathrm{T}}$ is the known initial disturbance. Note that the choice of $\boldsymbol{\phi}_{\mathrm{in}}$ is not arbitrary, it must satisfy the boundary conditions (16-17), as outlined in § 4. Due to the parabolic nature of the equations (15), it is not necessary to specify any boundary conditions at the outlet. Together with the boundary and initial conditions (16-17,18), the disturbance equations (15)

forms an initial-boundary-value problem that can be solved through a downstream marching procedure. A detailed description of the numerical scheme employed herein can be found in Hanifi *et al.* (1994).

4. Adjoint optimization procedure

We are interested in identifying the initial disturbance (18) that is optimal in the sense that it maximizes the growth of the disturbance energy, defined as

$$G = \frac{E_{\text{out}}}{E_{\text{in}}} \tag{19}$$

where E_{out} and E_{in} are the energy norms at the outlet and inlet of the considered chordwise domain. Here we follow the work of Hanifi *et al.* (1996) and Tumin & Reshotko (2003), who studied optimal disturbances in compressible, 2D boundary layers, and use the Mack energy norm (Mack (1969))

$$E_{\text{in}} = \int_0^{\xi^3_{\max}} \rho \left(|\hat{u}|^2 + |\hat{v}|^2 + |\hat{w}|^2 \right) \, \mathrm{d}\xi^3 \tag{20}$$

$$E_{\text{out}} = \int_0^{\xi^3_{\max}} \rho \left(|\hat{u}|^2 + |\hat{v}|^2 + |\hat{w}|^2 \right) + \frac{|\hat{T}|^2}{(\gamma - 1)\, T^2 M^2} \, \mathrm{d}\xi^3 \tag{21}$$

It should be noted that the energy norms presented here differs from those used by Tumin & Reshotko (2003) in the sense that all three velocity components are included. Tumin & Reshotko (2003) employed a method first suggested by Luchini (2000), valid in the high Reynolds-number limit, where the initial disturbance is confined to the cross-flow components and the optimization is carried out only with respect to the energy of the streamwise component at the outlet. Herein we follow the work by Andersson *et al.* (1999), and consider all three velocity components at both the inlet and the outlet.

We will employ an adjoint-based optimization procedure to identify the initial disturbance $\boldsymbol{\phi}_{\text{in}}$ which maximizes the energy growth (19). Such adjoint procedures were first utilized for studies of algebraic growth in spatially developing boundary layers by Andersson *et al.* (1999) and Luchini (2000), to which the interested reader is referred. An extensive study on this subject can also be found in the monograph by Schmid & Henningson (2001). Here, we will only outline the basic concepts of such procedures.

The initial-boundary value problem (15-18) is linear and homogeneous, and can be regarded as an input-output problem, where the disturbance equations (15) acts as a linear operator $\mathcal{A}$ on the initial disturbance $\boldsymbol{\phi}_{\text{in}}$ (the input) to produce a downstream disturbance $\boldsymbol{\phi}_{\text{out}}$ (the output) at the outlet

$$\boldsymbol{\phi}_{\text{out}} = \mathcal{A}\boldsymbol{\phi}_{\text{in}} \tag{22}$$

Employing operator theory, it can be shown that the maximum growth $G_{\max}$ is the largest eigenvalue $\lambda_{\max}$ of the eigenvalue problem

$$\mathcal{A}^*\mathcal{A}\boldsymbol{\phi} = \lambda\boldsymbol{\phi} \tag{23}$$

and the optimal initial disturbance $\boldsymbol{\phi}_{\text{in}}$ is the corresponding eigenvector $\boldsymbol{\phi}$. Here $\mathcal{A}^*$ represents the adjoint to the operator $\mathcal{A}$. To solve the eigenvalue problem (23) and determine the optimal disturbance, we employ power iterations of the form

$$\boldsymbol{\phi}^{n+1} = \mathcal{A}^*\mathcal{A}\boldsymbol{\phi}^n \tag{24}$$

The action of the operator $\mathcal{A}$ on an initial disturbance $\boldsymbol{\phi}^n$, i.e. $\mathcal{A}\boldsymbol{\phi}^n$, is given by the disturbance equations (15) and the boundary conditions (16-17). In order to perform the power iterations (24), we must however also determine the action of the adjoint operator $\mathcal{A}^*$. Remembering that $\mathcal{A}^*$ is the adjoint of the operator $\mathcal{A}$, which represents the disturbance equations (15), we derive the adjoint equations, as shown in appendix A

$$\tilde{\boldsymbol{A}}\boldsymbol{\phi}^* + \tilde{\boldsymbol{B}}\frac{\partial\boldsymbol{\phi}^*}{\partial\xi^3} + \tilde{\boldsymbol{C}}\frac{\partial^2\boldsymbol{\phi}^*}{\partial\xi^3\partial\xi^3} - \tilde{\boldsymbol{D}}\frac{\partial\boldsymbol{\phi}^*}{\partial\xi^1} = \boldsymbol{0}, \tag{25}$$

where $\boldsymbol{\phi}^* = (\rho^*, u^*, v^*, w^*, T^*)^{\mathrm{T}}$ are the adjoint variables and the matrices $\tilde{\boldsymbol{A}}$, $\tilde{\boldsymbol{B}}$, $\tilde{\boldsymbol{C}}$ and $\tilde{\boldsymbol{D}}$ are defined in appendix A. By considering the boundary terms obtained in the derivation of the adjoint equations (see appendix A), the following boundary conditions for the adjoint variables are imposed

$$u^* = v^* = w^* = T^* = 0 \quad \text{at} \quad \xi^3 = 0 \tag{26}$$

$$u^* = v^* = w^* = T^* = 0 \quad \text{at} \quad \xi^3 = \xi^3_{\max} \tag{27}$$

$$\tag{28}$$

The adjoint equations must be marched in the upstream direction. The initial conditions, derived in appendix A, must therefore be set at the outlet $\xi^1 = \xi^1_{\text{out}}$

$$\rho^* = -\rho\hat{w}d_{41}/\left(d_{11}d_{44}\right) \tag{29}$$

$$u^* = \rho\left(\hat{u} + \hat{w}d_{41}d_{12}/\left(d_{11}d_{44}\right) - \hat{w}d_{42}/d_{44}\right)/d_{22} \tag{30}$$

$$v^* = \rho\hat{v}/d_{33} \tag{31}$$

$$w^* = \rho\hat{w}/d_{44} \tag{32}$$

$$T^* = \hat{T}/\left((\gamma-1)\,T^2M^2d_{55}\right) \tag{33}$$

where d_{ii} denotes the ii element of the matrix $\boldsymbol{D}$, defined in appendix B. From the upstream solution of the adjoint equations at $\xi^1 = \xi^1_{\text{in}}$, a new candidate solution for the optimal disturbance is set, see equation (48-52) in appendix A. The initial disturbance $\hat{\boldsymbol{\phi}}_{in}$ is however constrained in the sense that it must satisfy the boundary conditions (16-17). Andersson *et al.* (1999) introduced a linear operator to enforce continuity, and included this constraint in the derivation of the adjoint system. It was shown that the procedure comes down to solving a least-square problem, where the candidate optimal disturbance obtained from the adjoint solution is replaced by the closest disturbance which satisfy continuity. Furthermore, Andersson *et al.* (1999) utilized the least-square fit to enforce the valid boundary conditions on the disturbance. Due to the complexity of deriving such a procedure for the compressible disturbance equations (15)

expressed in a non-orthogonal coordinate system, a more simplistic approach have been employed herein. As outlined in appendix A, the no-slip boundary conditions can be enforced by omitting one single term from the candidate initial disturbance (48-52). The modified initial disturbance, which satisfy the boundary conditions (16-17), is

$$\hat{\rho}_{\text{in}} = 0 \tag{34}$$

$$\hat{u}_{\text{in}} = \left(u^* d_{22} + w^* d_{44}\right)/\rho \tag{35}$$

$$\hat{v}_{\text{in}} = v^* d_{33}/\rho \tag{36}$$

$$\hat{w}_{\text{in}} = w^* d_{44}/\rho \tag{37}$$

$$\hat{T}_{\text{in}} = 0 \tag{38}$$

As seen in figure 7, the difference in energy growth between the candidate initial disturbance (48-52) and the modified initial disturbance (34-38) is well within 1%. In practise, the power iterations (24) is carried out as follows:

- step 1: The disturbance equations (15) is marched downstream. A starting guess for the initial disturbance $\boldsymbol{\phi}_{\text{in}}$ must be provided in the first iteration.
- step 2: The initial conditions for the adjoint equations at $\xi^1 = \xi^1_{\text{out}}$ is set from the downstream disturbance $\boldsymbol{\phi}_{\text{out}}$, according to (29-33).
- step 3: The adjoint equations (25) are marched in the upstream direction.
- step 4: The initial disturbances $\boldsymbol{\phi}_{\text{in}}$ is computed from the adjoint solution at $\xi^1 = \xi^1_{\text{in}}$, according to (34-38). The loop is restarted from step 1.

  The power iterations (step 1 - 4) are repeated until the energy growth is converged.

5. Results

5.1. *Verification*

The validity of the governing equations (15), derived for a non-orthogonal curvilinear coordinate system, was verified by a comparison with a previous study of the 2D Falkner–Skan boundary layer by Levin & Henningson (2003). This comparison also served to verify the implementation of the adjoint-based optimization procedure presented in § 4. Levin & Henningson (2003) calculated the optimal disturbances in three 2D meanflows subjected to chordwise pressure gradients of, respectively, $\beta_H = 0.1$, $\beta_H = 0.0$ and $\beta_H = -0.1$. Furthermore, they optimized the spanwise wavenumber and the chordwise positions where the disturbances were initiated in the boundary layer. The present implementation was employed to calculate the optimal disturbances and corresponding energy growth for these spanwise wavenumbers and chordwise intervals. The

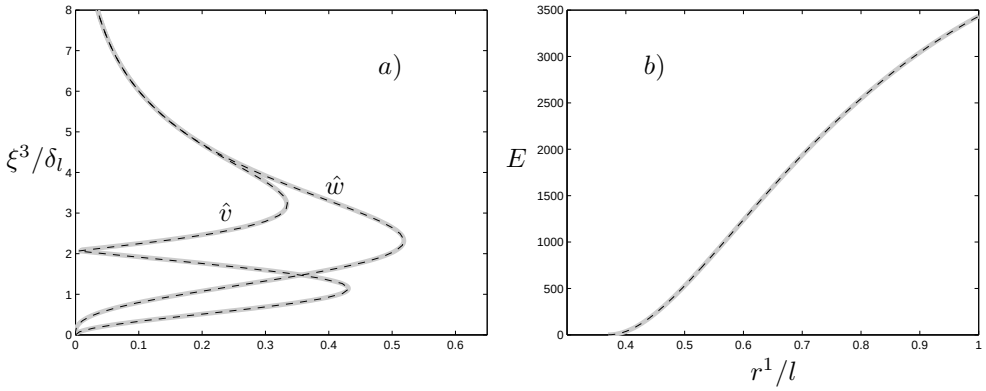

FIGURE 3. The optimal disturbance (a) and corresponding energy growth (b) in the Blasius boundary layer. Present implementation (dashed black line) with $\Lambda = 45°$, non-orthogonal coordinate system employed. Data from Levin & Henningson (2003) (grey line). The energy norm E is given by expression (21) in § 4.

results were in excellent agreement with the data from Levin & Henningson (2003).

The calculations in the 2D boundary layers described above were carried out with an orthogonal coordinate system. In order to verify the use of the non-orthogonal coordinate system, we consider the flow over a flat plate with zero pressure gradient, placed at an angle to the free-stream. This flow is a 2.5D boundary layer with a non-zero spanwise component when studied in the x reference frame, but reduces to the 2D Blasius boundary layer when studied in the r reference frame (see § 2). We can therefore compare results from the present implementation, where the non-orthogonal coordinate system ξ has been employed, to results from the 2D study by Levin & Henningson (2003). The angle between the streamwise axis ξ^1 and the spanwise axis ξ^2 is constant at $90° - \Lambda$ for this flow. Figure 3 shows the results from a calculation with $\Lambda = 45°$, and a comparison with data from Levin & Henningson (2003). Both the shape of the optimal disturbance and the corresponding energy growth are in close agreement. Sweep angles up to $\Lambda = 80°$ have been tested with equally good agreement. This comparative study verified that calculations with the non-orthogonal coordinate system ξ produces correct results, even when the angle between the horizontal coordinate axes ξ^1 and ξ^2 is as small as $10°$. Note that Levin & Henningson (2003) employed an optimization procedure valid in the high Reynolds-number-limit where the initial disturbance is constrained to the cross-flow components, i.e. the streamwise component of the initial disturbance is set to zero. Herein we follow Andersson *et al.* (1999) and consider

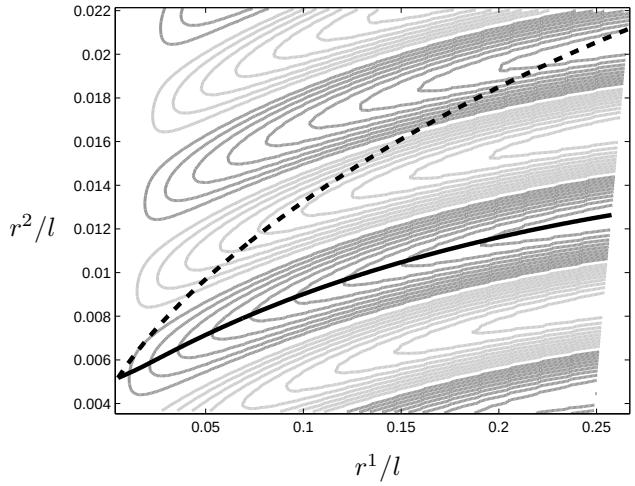

FIGURE 4. Contours of positive (dark gray) and negative (light gray) streamwise velocity. External streamline (dashed line) and the streakline (solid line) used in the calculations, following the maximum of the streamwise disturbance velocity. Note that the figure does not portray one plane at a fixed wall-normal position, but rather a curved sheet which follows the maximum of the streamwise disturbance velocity at each choordwise station. Note also the high visual aspect ratio between the r^1- and r^2-axis.

3D initial disturbances, as outlined in § 4. It was however shown by Andersson *et al.* (1999) that these two different optimization procedures produce the same result in the high Reynolds-number-limit.

5.2. *Integration path*

As outlined in § 3, the calculations are carried out under the assumption that the wavenumber is zero along the ξ^1 -axis. This axis is aligned with the external streamline, since it is known that disturbances in 3D boundary layers evolves nearly along this line. Calculations with the present implementation does however reveal that the disturbances are not perfectly aligned with the streamline, as seen in figure 4. This small deviation is equivalent to a small, but non-zero wavenumber with respect to the ξ^1-axis. Although such a small deviation will only cause neglectable errors locally, the cumulative effect may be significant when the disturbance equations (15) are integrated over a long streamwise distance. Furthermore, it was found that a small non-zero wavenumber makes the problem significantly harder to resolve. It is thus essential to identify and

align the ξ^1-axis with the propagation direction of the disturbances. Herein, we will define the disturbance trajectory as the line which follows the maximum of the streamwise disturbance velocity. This line will hereafter be denoted the *streakline*.

An iterative procedure was utilized to identify the streakline. As a first approximation, the external streamline serves as integration path and the optimal disturbance is calculated with the procedure described in § 4. The streakline is identified from the downstream development of the initial disturbance, and a new calculation is carried out along this new integration path. Once again the streakline is identified and a new calculation is carried out. This procedure was repeated until the streakline became fix. It was however found that the shape of the disturbances was rather insensitive to the choice of the integration path, only a few iterations was thus necessary. It must be stated that the streakline is not well defined in the small upstream part of the streamwise interval where the initial, vortical disturbance has yet to produce a sizable, well-defined streak. Different choices for the integration path over this small domain were tested, such as different extrapolations of the downstream, well-defined streakline. It was however found that the different choices of integration path in this small domain had no significant impact on the results. Furthermore it can be noted that another definition of the streakline was tested, defined as the line which follows the maximum disturbance energy based on the horizontal velocity components. This line was however found to coincide with that based on the maximum of the streamwise component, except in the small upstream region where the streak has yet to arise.

5.3. *Optimal disturbances and energy growth*

In this section we will study the optimal disturbances in boundary layers within the Falkner–Skan–Cooke family with a sweepangle of $\Lambda = 45°$. We consider both an accelerated flow with a chordwise pressure gradient of $\beta_{\mathrm{H}} = 0.1$ and a retarded flow; $\beta_{\mathrm{H}} = -0.05$. The chordwise velocity at the boundary layer edge (1) is chosen such that $\Phi = \Lambda = 45°$ at the chordwise position $r^1/l = 1$, where $R_l = U_l l/\nu = 10^6$ and $U_l = U_s\left(r^1 = l, r^3 = r^3_{\max}\right)$. We will employ two reference lengths for the presented figures, l and $\delta_l = \sqrt{\nu l/U_l}$.

Figure 5 presents the regions of exponential instability for stationary modes in the accelerated and retarded Falkner–Skan–Cooke boundary layers. In this section we will restrict our study of optimal disturbances to a sub-critical chordwise interval, $0.005 \leq r^1/l \leq 0.25$, in order to study purely transient growth. In § 5.4 we will extend this interval to super-critical flows and study the evolvement of algebraically growing, non-modal disturbances into exponentially amplified modes.

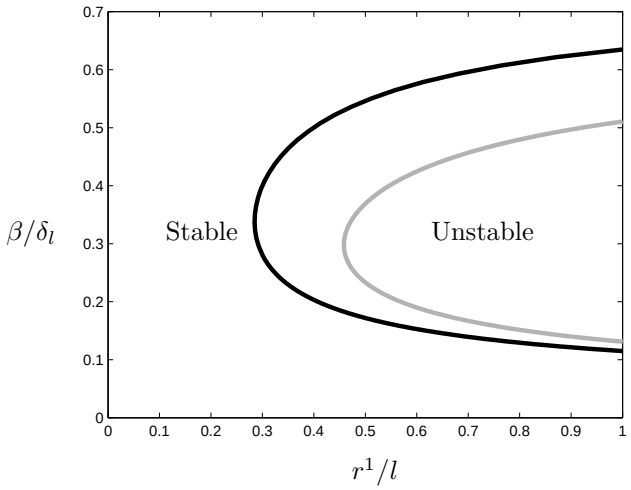

FIGURE 5. Neutral stability curve for stationary cross-flow modes in the Falkner–Skan–Cooke boundary layer at 45° sweepangle with favorable pressure gradient of $\beta_H = 0.1$ (black line) and adverse pressure gradient of $\beta_H = -0.05$ (grey line).

From a physical viewpoint it is desirable to start the calculations at the leading edge, in order to capture the process where vortical free-stream disturbances enters the boundary layer. There are however several problems associated with this upstream region. The Falkner–Skan–Cooke family of similarity solutions are discontinuous at the leading edge. For the normal velocity we have that $\lim_{r^1 \to 0} W \to \infty$, and in retarded flows it follows from equation (1) that $\lim_{r^1 \to 0} U^e \to \infty$. Despite these difficulties, which applies to the 2D case as well, Andersson *et al.* (1999) and Luchini (2000) independently carried out studies of transient growth in the Blasius boundary layer where the disturbances where introduced at the leading edge. Luchini (2000) utilized a jump condition to solve the singularity problem, while Andersson *et al.* (1999) carried out a study where the inception point was gradually moved towards the leading edge. They found that no dramatic changes occurs in the shape of the optimal disturbance or in the downstream response when the leading edge is approached, and concluded that the calculations could be initiated at the leading edge if the normal velocity is set to zero in the first calculation point. Neither Andersson *et al.* (1999) or Luchini (2000) did however address the problem that the boundary layer equations are not valid in this region. Levin & Henningson (2003), who studied optimal disturbances in the Falkner–Skan boundary layers with favorable, zero and adverse pressure gradients, optimized the point of inception. They found that the maximum growth occurs when the

disturbance is introduced into the boundary layer a significant distance downstream of the leading edge. The difficulties associated with the leading edge was therefore not considered.

For the swept flows studied herein, a new set of leading edge related problems arise in addition to those encountered in the 2D studies. The streamline angle, $\Phi = \arctan(V^e/U^e)$, is undefined at the leading edge in Falkner–Skan–Cooke boundary layers with non-zero pressure gradients. In accelerated flows we have $\lim_{r^1\to 0}\Phi = 90^\circ$, since $\lim_{r^1\to 0} U^e = 0$. The axes ξ^1 and ξ^2 of the non-orthogonal coordinate system will thus collapse at the leading edge. In retarded flows, where $\lim_{r^1\to 0} U_w \to \infty$, the limit of the streamline angle is $\lim_{r^1\to 0}\Phi = 0^\circ$. Both the accelerated and the retarded flow will undergo a very rapid transformation in the vicinity of the leading edge, where the streamline angle draws away from the extreme value at the leading edge. Furthermore, if it is assumed that the optimal disturbance takes the form of vortices more or less aligned with the external streamline, it is clear that the orientation of these vortices will vary rapidly when the point of inception is moved upstream towards the leading edge. Furthermore, the deviation of the streakline from the external streamline, described in § 5.2, is most severe near the leading edge.

Due to the difficulties discussed above, the point of inception was set a small distance downstream of the leading edge, at $r^1/L = 0.005$. Figure 6 presents the energy growth of the optimal disturbances as function of the spanwise wavenumber, for both the accelerated and the retarded flow over the chordwise interval $0.005 \leq r^1/l \leq 0.25$. As discussed in § 4, the initial disturbance is optimized to produce the maximum energy growth (19) over this interval. The figure also displays the level of convergence, since results calculated with both 1600 and 3200 chordwise points are included. We gather that the maximum transient growth in the accelerated flow occurs for $\beta/\delta_l = 0.54$, while the optimal spanwise wavenumber is $\beta/\delta_l = 0.57$ in the retarded flow. The retarded flow gives rise to twice the transient growth of the accelerated flow. Levin & Henningson (2003), who studied optimal disturbances in the 2D Falkner–Skan boundary layers, also found that retarded flows gives rise to higher transient growth. The energy growth of the optimal disturbances, with optimal wavenumbers, is shown as function of the coordinate r^1 in figure 7. A comparison between the initial disturbances with no-slip and un-physical boundary conditions is also shown, see § 4.

Figure 8 portrays the disturbance profiles of the optimal disturbances, with optimal spanwise wavenumber. As previously noted by Corbett & Bottaro (2001), who determined optimal disturbances in the Falkner–Skan–Cooke boundary layers within the temporal framework, the physical mechanism behind the transient growth is not evident from the modulus of the amplitude functions. In contrast to 2D boundary layers, the cross-flow component does not appear to have a sign shift. The physically relevant disturbance is however

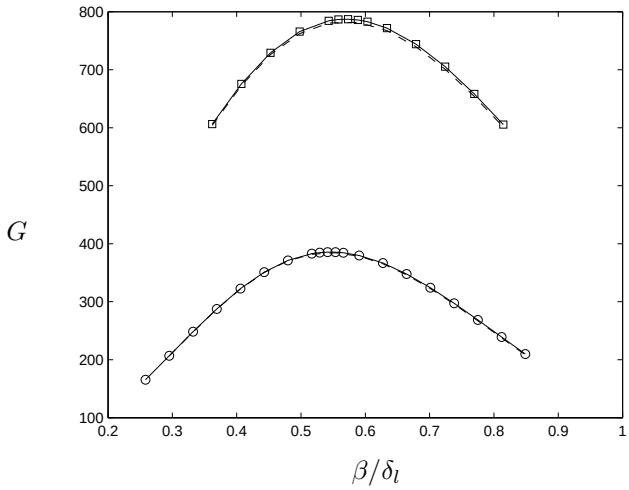

FIGURE 6. Energy growth of the optimal disturbances as function of the spanwise wavenumber β. Falkner–Skan–Cooke boundary layers with favorable (circles) and adverse (squares) pressure gradients of, respectively, $\beta_H = 0.1$ and $\beta_H = -0.05$. Growth over the interval $0.005 < r^1/l < 0.25$, calculated with 3200 points (solid line) and 1600 points (dashed line).

the real part of the total disturbance (14), which can also be written as

$$\tilde{q}_{\mathrm{R}} = \hat{q}_{\mathrm{R}} \cos(\beta\xi^2) - \hat{u}_{\mathrm{I}} \sin(\beta\xi^2) \tag{39}$$

where R and I denotes real and imaginary parts, respectively. A better perception of the physical situation can therefore be gained from figure 9 which shows a vector representation of the real part of the optimal disturbance in the cross-flow plane. It is apparent that the optimal disturbances take the form of counter-rotating vortices, similar to the optimal disturbances found in 2D flows. The vortices are however not symmetric as in 2D boundary layers, but tilted around the wall-normal axis. The vortices are tilted anti-clockwise in the accelerated flow and clockwise in the retarded flow. This difference is likely related to the cross-flow component of the boundary layer, which changes sign with the pressure gradient. As the disturbances evolve downstream their orientation changes, the streaks at the end of the interval are therefore tilted clockwise in the accelerated flow and anti-clockwise in the retarded flow, i.e. the opposite of the initial disturbance.

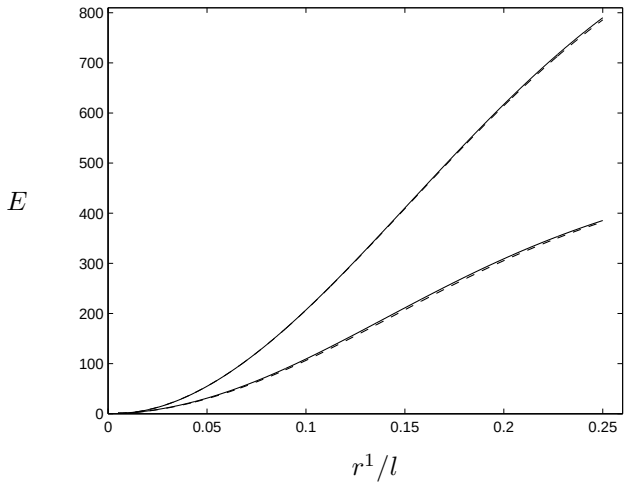

FIGURE 7. The upper curves show the energy growth of the optimal disturbance in the retarded flow ($\beta_H = -0.05$), the lower curves show the energy growth in the accelerated flow ($\beta_H = 0.1$). The dashed lines correspond to initial disturbances which satisfy no-slip boundary conditions while the solid lines corresponds to un-physical initial disturbances, see § 4.

5.4. *Non-modal and modal cross-flow disturbances*

In 2D boundary layers the regions of transient and modal growth are well separated in the (ω, R)-plane, as noted by Luchini (2000) in his study of transient growth in the Blasius boundary layer. The maximum transient growth occurs for stationary disturbances, and the growth decays rapidly with increasing frequency, while the exponential growth occurs for modal disturbances of relatively high frequencies. In 3D boundary layers no such separation exists, since stationary modes can receive exponential amplification. Stationary cross-flow modes are a more common cause of transition than their traveling counterparts in free-flight conditions (Reed & Saric (1989)). The stationary modes take the form of vortices, nearly aligned with the external streamline, and streaks of alternating high and low streamwise velocity. It is thus clear that this exponential instability resembles the algebraic instability described in § 5.3. This is contrary to the situation in 2D boundary layer, where the modal disturbances are traveling waves and bears little resemblance to the disturbances associated with algebraic instability.

In this section we will calculate the optimal disturbance in the accelerated flow, $\beta_{\mathrm{H}} = 0.1$, over the chordwise interval $0.005 \leq r^1/l \leq 1.0$, thus including

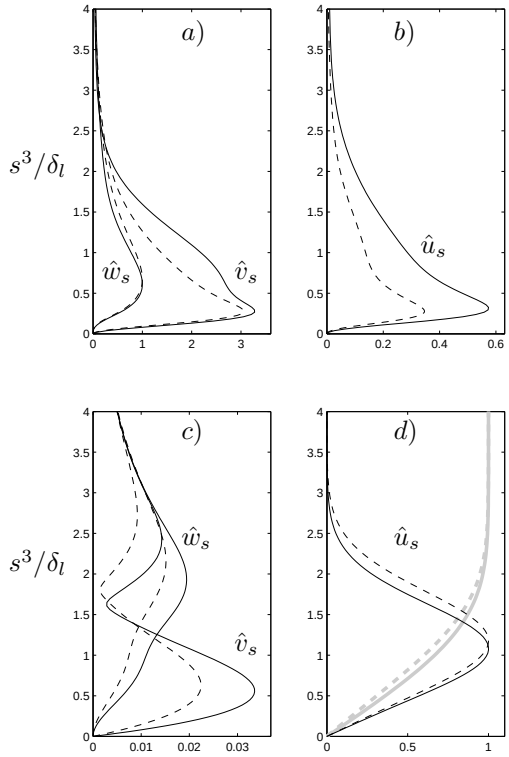

FIGURE 8. (a-b) Optimal disturbances in the Falkner–Skan–Cooke boundary layers at $r^1/l = 0.005$, $\beta_H = 0.1$ (solid line) and $\beta_H = -0.05$ (dashed line). All components normalized with $\hat{w}_{\max}$. (c-d) Downstream response to the optimal disturbance at $r^1/l = 0.25$, normalized with $\hat{u}_{\max}$. Falkner–Skan–Cooke profiles (grey line) included in (d).

super-critical flow. This allows us to study a scenario where transient growth pass over into exponential growth, to illuminate the differences and similarities between these instabilities. Corbett & Bottaro (2001) considered sub- and super-critical Reynolds-numbers, comparing algebraically growing disturbances to exponentially amplified eigenmodes. They concluded that the algebraically growing disturbances are fed into cross-flow eigenmodes as the critical Reynolds-number is exceeded. The temporal analysis employed by Corbett & Bottaro (2001) does however not allow a study where the downstream development of the disturbances can be monitored as they evolve from the sub- to

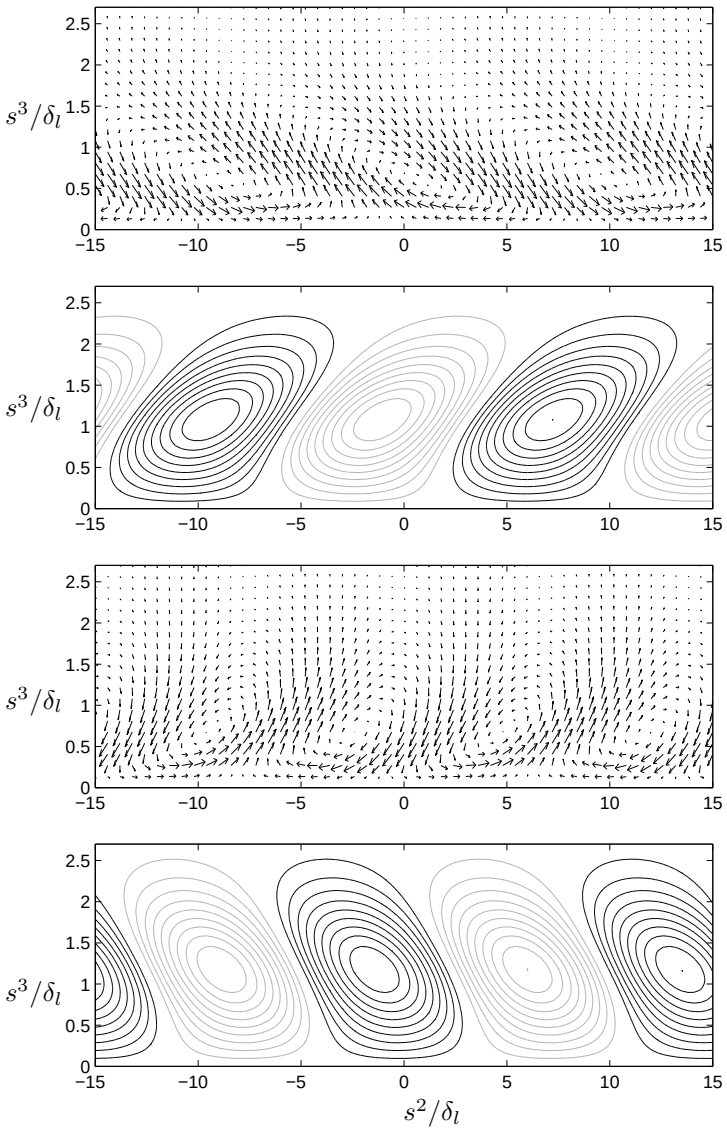

FIGURE 9. (a & c) Vector representation of optimal disturbances in the Falkner–Skan boundary layers, projected onto the cross-flow plane at $r^1/l = 0.005$. (c & d) Downstream response to the optimal disturbances at $r^1/l = 0.25$, contours of positive (black) and negative (grey) streamwise velocity in the cross-flow plane. (a & b): Favorable pressure gradient, $\beta_H = 0.1$. (c & d): Adverse pressure gradient, $\beta_H = -0.05$.

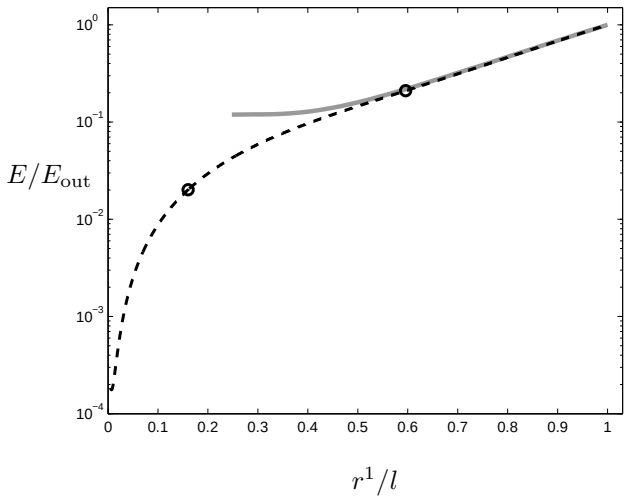

FIGURE 10. Energy growth of the optimal disturbance (black dashed line), algebraic growth followed by exponential growth. Data from a PSE calculation of a cross-flow mode (grey line) with the same spanwise wavenumber, $\beta/\delta_l = 0.34$, is included for comparison. The dots are associated with figure 12.

the super-critical domain of the boundary layer. The spatial approach applied herein will however allow such a study, where both the algebraic growth and the subsequent exponential amplification of the disturbances is investigated.

Figure 10 shows the energy growth of the optimal disturbance with the spanwise wavenumber $\beta = 0.34/\delta_l$. For comparison, we have included data from a PSE calculation of a cross-flow mode with the same wavenumber, initiated at the point of neutral stability. It is clear that the algebraic growth of the optimal disturbance is followed by exponential growth, where the growth rate collapse with that of the modal disturbance. The reason is apparent from figure 11 which presents the amplitude functions of the cross-flow mode as well as the downstream response of the optimal disturbance at the end of the streamwise interval, $r^1/l = 1.0$. The close agreement proves that the optimal disturbance has evolved into a cross-flow mode. From figure 10 it can be concluded that the transition from algebraic to exponential amplification is a gradual process without any jumps in the growth rate. Figure 12 portrays the amplitude functions at two streamwise stations, marked in figure 10, where the disturbances receives algebraic and exponential amplification, respectively. It is clear that no dramatic changes has occurred to the shape of the disturbance.

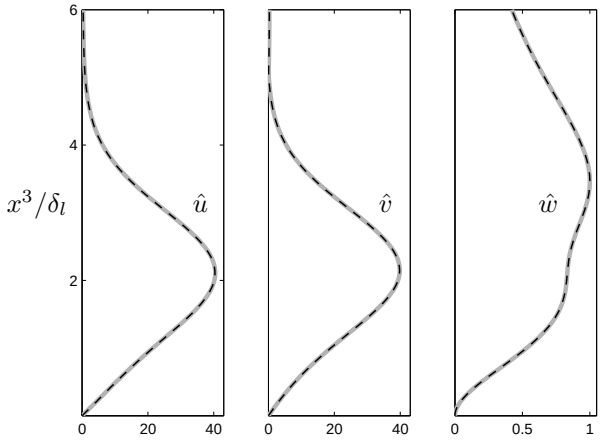

FIGURE 11. Downstream response to the optimal disturbance (dashed black line) at $r^1/l = 1.0$, compared to a PSE calculation of the cross-flow mode (grey line) with the same spanwise wavenumber, $\beta/\delta_l = 0.34$.

We thus conclude that the physical mechanism that drives the algebraic instability is similar to that responsible for the classical exponential instability, and that the algebraic disturbances are feed into exponentially amplified modes as the critical Reynolds-number is exceeded.

6. Conclusions

A parabolic set of disturbance equations were herein employed to study algebraic and exponential instability in the Falkner–Skan–Cooke boundary layer. An adjoint-based optimization procedure was utilized to identify optimal disturbances, i.e. the initial disturbance which receives the greatest amplification over a given chordwise interval. Two different flows were considered, one with a favorable chordwise pressure gradient of $\beta_{\mathrm{H}} = 0.1$ and one with an adverse pressure gradient of $\beta_{\mathrm{H}} = -0.05$. The sweepangle was set to $\Lambda = 45^\circ$, and the Reynolds number was set to $R_l = U_l l/\nu = 10^6$.

First a study was carried out over an interval restricted to sub-critical Reynolds numbers, $0.005 \leq r^1/l \leq 0.25$, where the growth of the initial disturbances is purely algebraic. It was found that the optimal disturbances takes the form of counter-rotating vortices when projected onto the cross-flow plane. The optimal spanwise wavenumbers were found to be $\beta/\delta_l = 0.54$ in the accelerated flow and $\beta/\delta_l = 0.57$ in the retarded flow. Contrary to findings from

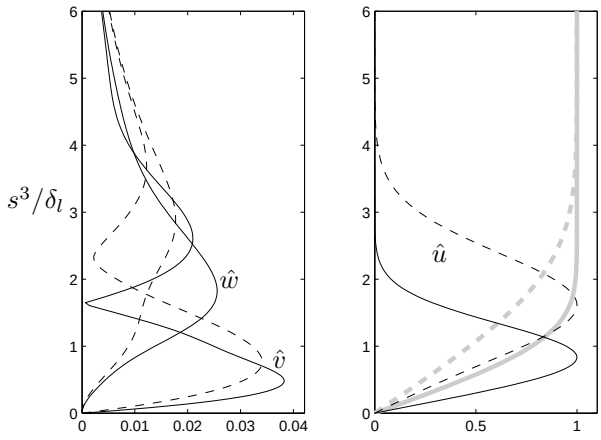

FIGURE 12. Downstream response to the optimal disturbance at $r^1/l = 0.16$ (solid line) and $r^1/l = 0.60$ (dashed line), i.e. the chordwise positions marked by dots in figure 10. Falkner–Skan–Cooke profiles at the same positions (grey line).

studies of optimal disturbances in 2D boundary layers, these vortices are not symmetrical about the wall-normal axis, but tilted in the cross-flow plane. As the disturbance evolves downstream, the direction of the tilting changes. The tilting is opposite in flows with favorable and adverse pressure gradient, since the cross-flow component of the Falkner–Skan–Cooke boundary layer changes sign with the pressure gradients.

Secondly, the optimal disturbance was calculated in the accelerated flow, $\beta_{\mathrm{H}} = 0.1$, over a chordwise interval which includes super-critical flow, $0.005 \leq r^1/l \leq 1.0$. The spatial analysis employed herein allowed a study of the disturbances as they evolved downstream, from the sub-critical region of algebraic growth into the classically unstable region of exponential amplification. It was shown that the disturbances are of the same basic shape in the regions where they receive algebraic and exponential amplification. Hence, it was concluded that similar physical mechanisms are responsible for both the algebraic and the exponential instability of the Falkner–Skan–Cooke boundary layer.

Acknowledgements

The financial support from the EU project TELFONA is gratefully acknowledged.

7. Appendix A

7.1. *Derivation of the adjoint equations*

The adjoint equations (25), are derived with respect to the inner product

$$(\boldsymbol{\psi}, \boldsymbol{\varphi}) = \int_0^{\xi^1_{\text{out}}} \int_0^{\xi^3_{\max}} \boldsymbol{\psi}^{\text{H}} \boldsymbol{\varphi} \quad \mathrm{d}\xi^3 \, \mathrm{d}\xi^1 \tag{40}$$

where $\boldsymbol{\psi}$ and $\boldsymbol{\varphi}$ are two arbitrary vector functions. Taking the inner product of the adjoint state vector $\boldsymbol{\phi}^*$ and the disturbance equations (15), and employing integration by parts to move the derivates from $\hat{\boldsymbol{\phi}}$ to $\boldsymbol{\phi}^*$, we arrive at

$$\begin{aligned}
\left(\boldsymbol{\phi}^*, \ \boldsymbol{A}\hat{\boldsymbol{\phi}} + \boldsymbol{B}\frac{\partial \hat{\boldsymbol{\phi}}}{\partial \xi^3} + \boldsymbol{C}\frac{\partial^2 \hat{\boldsymbol{\phi}}}{\partial \xi^3 \partial \xi^3} + \boldsymbol{D}\frac{\partial \hat{\boldsymbol{\phi}}}{\partial \xi^1} \right) = \\
\left(\tilde{\boldsymbol{A}}\boldsymbol{\phi}^* + \tilde{\boldsymbol{B}}\frac{\partial \boldsymbol{\phi}^*}{\partial \xi^3} + \tilde{\boldsymbol{C}}\frac{\partial^2 \boldsymbol{\phi}^*}{\partial \xi^3 \partial \xi^3} - \tilde{\boldsymbol{D}}\frac{\partial \boldsymbol{\phi}^*}{\partial \xi^1}, \ \hat{\boldsymbol{\phi}} \right) + \\
\int_0^{\xi^1_{\text{out}}} \left[\boldsymbol{\phi}^{*\text{H}} \left(\boldsymbol{B} - \frac{\partial \boldsymbol{C}}{\partial \xi^3} \right) \hat{\boldsymbol{\phi}} + \frac{\partial \boldsymbol{\phi}^{*\text{H}}}{\partial \xi^3} \boldsymbol{C}\hat{\boldsymbol{\phi}} + \boldsymbol{\phi}^{*\text{H}} \boldsymbol{C} \frac{\partial \hat{\boldsymbol{\phi}}}{\partial \xi^3} \right]_0^{\xi^3_{\max}} \mathrm{d}\xi^1 + \\
\int_0^{\xi^3_{\max}} \left[\boldsymbol{\phi}^{*\text{H}} \boldsymbol{D} \hat{\boldsymbol{\phi}} \right]_0^{\xi^1_{\text{out}}} \mathrm{d}\xi^3
\end{aligned} \tag{41}$$

where the matrices of the adjoint equations (25) are defined as

$$\tilde{\boldsymbol{A}} = \boldsymbol{A}^{\text{H}} - \frac{\partial \boldsymbol{B}^{\text{H}}}{\partial \xi^3} + \frac{\boldsymbol{C}^{\text{H}}}{\partial \xi^3 \partial \xi^3} - \frac{\boldsymbol{D}^{\text{H}}}{\partial \xi^1} \tag{42}$$

$$\tilde{\boldsymbol{B}} = -\boldsymbol{B}^{\text{H}} + 2\frac{\partial \boldsymbol{C}^{\text{H}}}{\partial \xi^3} \tag{43}$$

$$\tilde{\boldsymbol{C}} = \boldsymbol{C}^{\text{H}} \tag{44}$$

$$\tilde{\boldsymbol{D}} = \boldsymbol{D}^{\text{H}}. \tag{45}$$

and the superscript H denotes conjugate transpose. The left-hand side and the first term of the right-hand side of equation (41) are both zero, since these inner products include the disturbance equations (15) and the adjoint equations (25), respectively. The boundary terms, i.e. the remainder of the right-hand side, must therefore also be zero. We thus have

$$\int_0^{\xi^1_{\text{out}}} \left[\boldsymbol{\phi}^{*\text{H}} \left(\boldsymbol{B} - \frac{\partial \boldsymbol{C}}{\partial \xi^3} \right) \hat{\boldsymbol{\phi}} + \frac{\partial \boldsymbol{\phi}^{*\text{H}}}{\partial \xi^3} \boldsymbol{C}\hat{\boldsymbol{\phi}} + \boldsymbol{\phi}^{*\text{H}} \boldsymbol{C} \frac{\partial \hat{\boldsymbol{\phi}}}{\partial \xi^3} \right]_0^{\xi^3_{\max}} \mathrm{d}\xi^1 = 0 \tag{46}$$

$$\int_0^{\xi^3_{\max}} \left[\boldsymbol{\phi}^{*\text{H}} \boldsymbol{D} \hat{\boldsymbol{\phi}} \right]_0^{\xi^1_{\text{out}}} \mathrm{d}\xi^3 = 0 \tag{47}$$

Introducing the boundary conditions of the state variables (16-17) into (46), we can determine the boundary conditions for the adjoint variables (28) as

$$u^* = v^* = w^* = T^* = 0 \quad \text{at} \quad \xi^3 = 0$$
$$u^* = v^* = w^* = T^* = 0 \quad \text{at} \quad \xi^3 = \xi^3_{\max}$$

Furthermore, by identifying the energy norms (20-21) in the boundary term (47) we can determine the initial conditions (29-33) for the adjoint equations

$$\rho^* = -\rho\hat{w}d_{41}/\left(d_{11}d_{44}\right)$$
$$u^* = \rho\left(\hat{u} + \hat{w}d_{41}d_{12}/\left(d_{11}d_{44}\right) - \hat{w}d_{42}/d_{44}\right)/d_{22}$$
$$v^* = \rho\hat{v}/d_{33}$$
$$w^* = \rho\hat{w}/d_{44}$$
$$T^* = \hat{T}/\left(\left(\gamma-1\right)T^2M^2d_{55}\right)$$

and the optimal initial conditions (34-34) for the state equations

$$\hat{\rho} = 0 \tag{48}$$
$$\hat{u} = \left(\rho^*d_{12} + u^*d_{22} + w^*d_{44}\right)/\rho \tag{49}$$
$$\hat{v} = v^*d_{33}/\rho \tag{50}$$
$$\hat{w} = w^*d_{44}/\rho \tag{51}$$
$$\hat{T} = 0 \tag{52}$$

The term ρ^*d_{12}/ρ in (49) must however be omitted in order to satisfy the boundary conditions (16), as discussed in § 4. Further details on the adjoint Nolot-code can be found in Pralits *et al.* (2001).

8. Appendix B. Operator matrices

The non-zero components of the matrices $\boldsymbol{A}$, $\boldsymbol{B}$, $\boldsymbol{C}$ and $\boldsymbol{D}$ in equation (15) are

$a\left(1,1\right) = D_3\left(W\right) + \tilde{c}D_1\left(U\right) + i\beta\left(V - \tilde{t}U\right)$
$a\left(1,2\right) = \tilde{c}D_1\left(\rho\right) - i\tilde{t}\beta\rho$
$a\left(1,3\right) = i\beta\rho$
$a\left(1,4\right) = D_3\left(\rho\right)$
$a\left(2,1\right) = D_1\left(U\right)U + D_3\left(U\right)W - \frac{i\tilde{t}\beta}{\gamma M^2}T$
$a\left(2,2\right) = \rho\left(\tilde{c}D_1\left(U\right) + i\beta\left(V - \tilde{t}U\right)\right) + \frac{\mu}{R}\beta^2\left(1 + \tilde{t}^2l_2\right)$
$a\left(2,3\right) = -\frac{\mu}{R}\tilde{t}l_1\beta^2$
$a\left(2,4\right) = \rho D_3\left(U\right) + \frac{i}{R}\frac{\mathrm{d}\mu}{\mathrm{d}T}\tilde{t}\beta D_3\left(T\right)$
$a\left(2,5\right) = \frac{-i}{\gamma M^2}\tilde{t}\beta\rho + \frac{1}{R}\left(\frac{\mathrm{d}\mu}{\mathrm{d}T}\left(-D_{33}\left(U\right) + i\tilde{t}l_0\beta D_3\left(W\right)\right) - D_3\left(U\right)\frac{\mathrm{d}^2\mu}{\mathrm{d}T^2}D_3\left(T\right)\right)$
$a\left(3,1\right) = U\tilde{c}D_1\left(V\right) + D_3\left(V\right)W + \frac{i\beta}{\gamma M^2}T$
$a\left(3,2\right) = \rho\tilde{c}D_1\left(V\right) - \frac{\mu l_1\tilde{t}}{R}\beta^2$
$a\left(3,3\right) = \rho i\beta\left(V - \tilde{t}U\right) + \frac{\mu}{R}\beta^2\left(l_2 + \tilde{t}^2\right)$
$a\left(3,4\right) = \rho D_3\left(V\right) - \frac{i\beta}{R}\frac{\mathrm{d}\mu}{\mathrm{d}T}D_3\left(T\right)$

$$a(3,5) = \frac{i\beta}{\gamma M^2}\rho + \frac{1}{R}\left(-\frac{\mathrm{d}\mu}{\mathrm{d}T}\left(D_{33}(V) + il_0\beta D_3(W)\right) - D_3(V)\frac{\mathrm{d}^2\mu}{\mathrm{d}T^2}D_3(T)\right)$$
$$a(4,1) = D_3(W)W + \tilde{c}D_1(W)U + \frac{1}{\gamma M^2}D_3(T) +$$
$$\frac{\mu}{R}\frac{l_2}{\rho}\left(D_{33}(W) + \tilde{c}D_{13}(U) + i\beta\left(D_3(V) - D_3(U)\tilde{t}\right)\right)$$
$$a(4,2) = \rho\tilde{c}D_1(W) + \frac{1}{R}\left(il_0D_3(T)\frac{\mathrm{d}\mu}{\mathrm{d}T}\beta\tilde{t} + \frac{\mu l_2}{\rho}\left(\tilde{c}D_{13}(\rho) - iD_3(\rho)\beta\tilde{t}\right)\right)$$
$$a(4,3) = -\frac{i\beta}{R}l_0\frac{\mathrm{d}\mu}{\mathrm{d}T}D_3(T) + \frac{D_3(\rho)}{\rho}\frac{i\beta}{R}\mu l_2$$
$$a(4,4) = \rho\left(D_3(W) + i\beta\left(V - \tilde{t}U\right)\right) + \frac{1}{R}\mu\beta^2\left(1 + \tilde{t}^2\right) + \frac{D_{33}(\rho)}{\rho}\frac{\mu}{R}l_2$$
$$a(4,5) = \frac{1}{\gamma M^2}D_3(\rho) +$$
$$\frac{1}{R}\left(-D_3(W)D_3(T)\frac{\mathrm{d}^2\mu}{\mathrm{d}T^2}l_2 + \frac{\mathrm{d}\mu}{\mathrm{d}T}\left(-D_{33}(W)l_2 + i\beta\left(-D_3(V) + \tilde{t}D_3(U)\right)\right)\right)$$
$$a(5,1) = \frac{\gamma-1}{\gamma}\left(WD_3(T) + iT\beta V + \tilde{t}\beta U\right) + c_p\left(-WD_3(T) - \tilde{c}UD_1(T)\right)$$
$$a(5,2) = (\gamma-1)M^2\left(\tilde{c}D_1(p) - 2\frac{i\mu}{R}l_0\beta D_3(W)\right) - \rho c_p\tilde{c}D_1(T)$$
$$a(5,3) = -2\frac{i\mu}{R}l_0\beta(\gamma-1)M^2D_3(W)$$
$$a(5,4) = (\gamma-1)M^2\frac{2i\mu}{R}\beta\left[D_3(V) - \tilde{t}D_3(U)\right] - \rho c_pD_3(T)$$
$$a(5,5) = \rho\left(\frac{\mathrm{d}c_p}{\mathrm{d}T}\left(-WD_3(T) - U\tilde{c}D_1(T)\right) + i\left[\frac{\gamma-1}{\gamma} - c_p\right]\beta\left(V - \tilde{t}U\right)\right) +$$
$$\frac{1}{R\mathrm{Pr}}\left[\frac{\mathrm{d}\kappa}{\mathrm{d}T}D_{33}(T) + \frac{\mathrm{d}^2\kappa}{\mathrm{d}T^2}\left(D_3(T)\right)^2 - \kappa\beta^2\left(\tilde{t}^2 + 1\right)\right] +$$
$$\frac{\gamma-1}{R}\frac{\mathrm{d}\mu}{\mathrm{d}T}M^2\left[\left(D_3(U)\right)^2 + \left(D_3(V)\right)^2 + l_2\left(D_3(W)\right)^2\right] +$$
$$\frac{\gamma-1}{\gamma}WD_3(\rho)$$
$$b(1,1) = W$$
$$b(1,4) = \rho$$
$$b(2,2) = \rho W - \frac{1}{R}\frac{\mathrm{d}\mu}{\mathrm{d}T}D_3(T)$$
$$b(2,4) = i\tilde{t}\beta\frac{\mu}{R}l_1$$
$$b(2,5) = -\frac{1}{R}D_3(U)\frac{\mathrm{d}\mu}{\mathrm{d}T}$$
$$b(3,3) = \rho W - \frac{1}{R}\frac{\mathrm{d}\mu}{\mathrm{d}T}D_3(T)$$
$$b(3,4) = -\frac{i\mu}{R}\beta l_1$$
$$b(3,5) = -\frac{1}{R}D_3(V)\frac{\mathrm{d}\mu}{\mathrm{d}T}$$
$$b(4,1) = \frac{1}{\gamma M^2}T + \frac{\mu}{R}\frac{l_2}{\rho}\left(2D_3W + \tilde{c}D_1U + i\beta V - \tilde{t}\beta U\right)$$
$$b(4,2) = \frac{\mu}{R}\left(\frac{l_2}{\rho}D_1\rho - i\beta\tilde{t}\right)$$
$$b(4,3) = \frac{i\mu}{R}\beta$$
$$b(4,4) = \rho W + \frac{l_2}{R}\left(2\mu\frac{D_3(\rho)}{\rho} - \frac{\mathrm{d}\mu}{\mathrm{d}T}D_3(T)\right)$$
$$b(4,5) = \frac{1}{\gamma M^2}\rho - \frac{l_2}{R}\frac{\mathrm{d}\mu}{\mathrm{d}T}D_3(W)$$
$$b(5,1) = \frac{\gamma-1}{\gamma}WT$$
$$b(5,2) = 2(\gamma-1)M^2\frac{\mu}{R}D_3(U)$$
$$b(5,3) = 2(\gamma-1)M^2\frac{\mu}{R}D_3(V)$$
$$b(5,2) = 2(\gamma-1)M^2\frac{\mu}{R}l_2D_3(W)$$
$$b(5,5) = \rho W\left[\frac{\gamma-1}{\gamma} - c_p\right] + \frac{2}{R\mathrm{Pr}}\frac{\mathrm{d}\kappa}{\mathrm{d}T}D_3(T)$$

$c\left(2,2\right) = -\frac{\mu}{R}$
$c\left(3,3\right) = -\frac{\mu}{R}$
$c\left(4,1\right) = l_2 \frac{\mu}{R\rho} W$
$c\left(5,5\right) = \frac{\kappa}{R\mathrm{Pr}}$
$d\left(1,1\right) = \tilde{c}U$
$d\left(1,2\right) = \tilde{c}\rho$
$d\left(2,2\right) = \tilde{c}\rho U$
$d\left(3,3\right) = \tilde{c}\rho U$
$d\left(4,1\right) = \tilde{c} l_2 \frac{\mu}{\rho R} D_3 U$
$d\left(4,2\right) = \tilde{c} l_2 \frac{\mu}{\rho R} D_3 \rho$
$d\left(4,4\right) = \tilde{c}\rho U$
$d\left(5,5\right) = -\tilde{c} c_p \rho U$
where $\tilde{c} = 1/\cos\left(\Phi\right), \quad \tilde{t} = \tan\left(\Phi\right), \quad D_i = \frac{\partial}{\partial \xi^i}, \quad D_{ij} = \frac{\partial^2}{\partial \xi^i \partial \xi^j}$ and $l_j = \frac{\lambda}{\mu} + j$

References

Andersson, P., Berggren, M. & Henningson, D. 1999 Optimal disturbances and bypass transition in boundary layers. *Phys. Fluids* **11** (1), 134–150.

Bagheri, S. & Hanifi, A. 2007 The stabilizing effect of streaks on TS waves and oblique waves: A parametric study. To be published in *Phys. Fluids*.

Butler, K. & Farrell, V. 1992 Three-dimensional optimal pertubations in viscous shear flow. *Phys. Fluids A* **4** (8), 1637–1650.

Cooke, J. C. 1950 The boundary layer of a class of infinite yawed cylinders. *Proc. Camb. Phil. Soc* **46**, 645–648

Corbett, P. & Bottaro, A. 2001 Optimal linear growth in swept boundary layers. *J. Fluid Mech* **435**, 1–23.

Ellingsen, T. & Palm, E. 1975 Stability of linear flow. *Phys. Fluids* **18** (4), 487–488.

Farrell, B. 1988 Optimal exitation of pertubations in viscous shear flow. *Phys. Fluids* **31** (8), 2093–2102.

Floryan, J. & Saric, W. 1979 Stability of Görtler vortices in boundary layers. *AIAA J.* **20** (3), 316–324.

Hall, P. 1983 The linear development of Görtler vortices in growing boundary layers. *J. Fluid Mech.* **130**, 41–58.

Hanifi, A., Schmid, P. & Henningson, D. S 1996 Transient growth in compressible boundary layer flow. *Phys. Fluids* **8** (3), 826–837.

Hanifi, A., Henningson, D. S., Hein, S. & Bertolotti, F. P. 1994 'Linear Nonlocal Instability Analysis - the linear NOLOT code'. *FFA TN* 1994-54, See also Hein et al. 1994.

Henningson, D., Lundbladh, A. & Johansson, A. 1993 A mechanism for bypass transition from localized disturbances in wall-bounded shear flows. *J. Fluid Mech.* **250**, 169–238.

Högberg, M. & Henningson, D. S. 1998 Secondary instability of cross-flow vortices in Falkner–Skan–Cooke boundary layers. *J. Fluid Mech.* **368**, 339–357.

Hultgren, L. & Gustavsson, L. 1981 Algebraic growth of disturbances in a laminar boundary layer. *Phys. Fluids* **24** (6), 1000–1004.

Klebanoff, P. 1971 Effect of freestream turbulence on the laminar boundary layer. *Bull. Am. Phys. Soc.* **10**, 1323.

Landahl, M. T. 1975 Wave breakdown and turbulence. *SIAM J. Appl. Maths.***28** (4), 735–756.

Landahl, M. T. 1980 A note on an algebraic instability of inviscid parallel shear flows. *J. Fluid Mech.* **98** (2), 243–251.

Levin, O. & Henningson, D. S. 2003 Exponential vs algebraic growth and transition prediction in boundary layer flow. *Flow, Turbulence and Combustion* **70**, 183–210.

Luchini, P. 1996 Reynolds-number-independent instability of the boundary layer over a flat surface. *J. Fluid Mech.* **327**, 101–115.

Luchini, P. 2000 Reynolds-number-independent instability of the boundary layer over a flat surface: optimal perturbations. *J. Fluid Mech.* **404**, 289–309.

Mack, L. M. 1969 Boundary layer stability theory. Jet Propulsion Lab., JPL Rept. 99-277, California Inst. of Technology, Pasadena, CA, Nov. 1969.

Matsubara, M. & Alfredsson, P. 2001 Disturbance growth in boundary layers subjected to free-stream turbulence. *J. Fluid Mech.* **430**, 149–168.

Pralits, J.0, Airiau, C., Hanifi, A. & Henningson, D.S 2001 Sensitivity Analysis Using Adjoint Parabolized Stability Equations for Compressible Flows. *Flow, Turbulence and Combustion.* **65**, 321–346.

Radeztsky, R. H., Reibert, M. S. & Saric, W. S. 1999 Effect of isolated micron-sized roughness on transition in swept-wing flows. *AIAA J.* **37**, 1370-1377.

Reddy, S. & Henningson, D. 1993 Energy growth in viscous channel flows. *J. Fluid Mech.* **252**, 209–238.

Reed, H. L. & Saric, W. S. 1989 Stability of three-dimensional boundary layers. *Ann. Rev. Fluid. Mech* **21**, 235–284.

Schlichting, H. 1979 Boundary-Layer Theory, 7th Edition, Mc-GRAW HILL

Schmid, P. J. & Henningson, D. S. 2001 Stability and transition in shear flows, Springer.

Trefethen, L. N., Trefethen, A. E., Reddy, S. C. & Driscoll, T. A. 1993 Hydrodynamic stability without eigenvalues. *Science* **261**, 578 - 584.

Tumin, A. & Reshotko, E. 2003 Optimal disturbances in compressible boundary layers. *AIAA Paper* 2003-0792.